International Journal for Uncertainty Quantification, 3 (1): 73–100 (2013)

VALIDATION OF A PROBABILISTIC MODEL FOR MESOSCALE ELASTICITY TENSOR OF RANDOM POLYCRYSTALS

Arash Noshadravan,[1,*] Roger Ghanem,[1] Johann Guilleminot,[2] Ikshwaku Atodaria,[3] & Pedro Peralta[3]

[1] *University of Southern California, Department of Civil and Environmental Engineering, Los Angeles, California 90089-2531, USA*

[2] *Université Paris-Est, Laboratoire Modélisation et Simulation Multi Echelle, MSME, Marne la Vallée, France*

[3] *Arizona State University, School for Engineering of Matter, Transport and Energy, Tempe, Arizona 85287-6106, USA*

Original Manuscript Submitted: 08/25/2011; Final Draft Received: 11/08/2011

In this paper, we present validation of a probabilistic model for mesoscale elastic behavior of materials with microstructure. The linear elastic constitutive matrix of this model is described mathematically as a bounded random matrix. The bounds reflect theoretical constraints consistent with the theory of elasticity. We first introduce a statistical characterization of an experimental database on morphology and crystallography of polycrystalline microstructures. The resulting statistical model is used as a surrogate to further experimental data, required for calibration and validation. We then recall the construction of a probabilistic model for the random matrix characterizing the apparent elasticity tensor of a heterogeneous random medium. The calibration of this coarse scale probabilistic model using an experimental database of microstructural measurements and utilizing the developed microstructural simulation tool is briefly discussed. Before using the model as a predictive tool in a system level simulation for the purpose of detection and prognosis, the credibility of the model must be established through evaluating the degree of agreement between the predictions of the model and the observations. As such, a procedure is presented to validate the probabilistic model from simulated data resulting from subscale simulations. Suitable quantities of interest are introduced and predictive accuracy of the model is studied by comparing probability density functions of response quantities of interest. The validation task is exercised under both static and dynamic loading condition. The results indicate that the probabilistic model of mesoscale elasticity tensor is adequate to predict the response quantity of interest in the elastostatic regime. The scatter in the model predictions is found to be consistent with the fine scale response. In the case of elastodynamic, the model predicts the mean behavior for lower frequency for which we have a quasistatic regime.

KEY WORDS: *stochastic modeling, multiscale modeling, heterogeneous random media, model validation and verification, polycrystalline microstructure*

1. INTRODUCTION

Classical theories of material behavior that involve the concept of a homogenized continuum are often too idealized to reflect the inherent complexities in the structure of many engineering materials such as composites, polycrystals, granular materials, and concrete. Regardless of the differences in the nature of heterogeneities, these materials all share a common characteristic which is the presence of an underlying microstructure. There is often complex vari-

*Correspond to Arash Noshadravan, E-mail: noshadra@usc.edu

2152–5080/13/$35.00

ability in the size, shape, and spatial configuration of microstructural constituents. Multiple physical processes, which occur at the level of microstructure, typically govern the constitutive behavior and damage nucleation of materials. The theory of random heterogeneous material has undergone a profound development over the past four decades since the pioneering work of Hill [1], which subsequently led to the theories and techniques for computing bounds for overall properties [2–7]. These theories rely on the concept of an *effective property* that describes the relationship between appropriate averages of mechanical fields. The effective properties are theoretically defined under certain assumptions and conditions on the constitution of the material (see [4, 8] for instance). A fundamental prerequisite on the validity of the effective properties is the existence of a representative volume element (RVE), i.e., a volume element that is large enough compared to the average size of microscale constituents, and small enough with respect to the macroscale dimensions for which the structural application is carried out. This condition is classically referred to as *separation of scales*. The overall properties, in this case, are assumed to exhibit a negligible level of statistical fluctuation and the deterministic framework detailed in the classical literature can be suitable for modeling the heterogeneous medium. However, there are other classes of problems in which the characterization needs to be carried out at a mesoscale, that is, a domain whose characteristic length is smaller than the RVE. A volume element at this scale is referred to as a statistical volume elements (SVE), whose overall properties exhibit a considerable amount of statistical fluctuations. Taking into account these fluctuations is of significant importance in describing the scatter observed at the macroscale for some physical behavior of interest, e.g., fatigue life in metallic structures, which is directly linked to the phenomena occurring at the scale of heterogeneity. Hence, a mechanistic model should adequately accommodate the mesoscale fluctuations in order to be suitable for predicting such behavior. For these classes of problems, the deterministic framework underlying the classical concept of effective properties is inadequate. Nondeterministic approaches are thus required to take into account the scatter in the mechanical behavior.

Over the past decade, the area of stochastic multiscale modeling has gained significant attention for analyzing and predicting the behavior of complex material. The present work is motivated by two challenges in modeling and simulating multiscale behavior. The first one is concerned with the construction of a sufficiently representative description of random media in terms of morphology and material properties, for an intended purpose. The construction of this representation often requires a compromise such that it avoids redundant details while carrying as much relevant information on fine scale features as needed for the analysis of the targeted physical phenomena. The second important challenge arises in modeling the relationship between the random microheterogeneities and the parameters or functions used to describe the physical processes of interest at the coarse scale. One of the essential questions in this regard is whether the coarse scale description is capable of capturing the signature of fine scale characteristics. The inherent heterogeneities in the nature of these fine scale features are reflected on coarse scale observables in the form of random fluctuations around the average response. Hence, any multiscale mechanistic model must account for these fluctuations in order to capture the effect of subscale heterogeneities. There are essential characteristics for such a mechanistic model of material behavior that make it suitable to be used as a predictive tool. A model needs to be adopted such that the state of the model is amenable to comparison to experimental observables and the model behavior is sensitive to the subscale heterogeneities. Moreover, the scatter in the predictions of the model needs to be consistent with the observed scatter.

The present paper aims at addressing the second characteristic identified above and is concerned with the validation of a stochastic mechanistic model at the coarse scale. The model is established within the framework of the so-called nonparametric approach for uncertainties [9, 10]. Making use of the maximum entropy (MaxEnt) principle, a probabilistic model is identified to describe the mechanical system characterized by fourth-order elasticity tensor that is constrained by a pair of physics-based bounds. The matrix representation of the fourth-order elasticity tensor is modeled as a random matrix, exhibiting fluctuations that are connected to fine scale features through a calibration process performed using a micromechanical framework. The details of the model construction are presented elsewhere [11] and will be briefly reviewed in this article. Integrating such a description into a damage mechanics framework, could be useful in capturing the signature of the microlevel defect that contributes in damage evolution and fatigue cracks in metallic structures. Before using the model as a predictive tool in a system level simulation for the purpose of detection and prognosis, however, the credibility of the model must be established through evaluating the degree of agreement between the predictions of the model and the observations. This step constitutes the main goal of this article.

The experimental calibration and validation of the model will require testing of a statistically meaningful number of samples possessing statistically similar microstructures. Experimental samples, if available, are often not sufficient in number due to the time constraint as well as the experimental cost and burden. As such, the first part of the paper is devoted to developing an efficient experimentally based simulation tool for digitally generating statistical ensembles of microstructures that are consistent with the available experimental data in a prescribed statistical sense. Such simulations ensure a reasonable level of convergence in the process of identification of the probabilistic model of the coarse scale material description. The resulting microstructures are also used to generate model-based measurements in the validation stage.

This paper is organized as follows: In Section 2 we address the construction of a statistical model for characterization and realization of two-dimensional (2D) polycrystalline microstructures from the available microstructural measurements. The resulting statistical model is used as a surrogate to further experimental data, required for calibration and validation of a probabilistic model for the mesoscale behavior of material with microstructure. In Section 3 we recall the construction and identification of a probabilistic model for the mesoscale behavior of material with microstructure. The linear elastic constitutive matrix of this model is described mathematically as a random matrix that is bounded, in a deterministic sense, from above and below. Finally, in Section 4, we present a validation procedure for the predictive behavior of the probabilistic mesoscale model by comparing the scatter in the predictions of a response quantity of interest with the observed scatter obtained from fine scale simulations. The validation task is exercised for the elastostatic as well as the elastodynamic regime.

2. STATISTICAL MODEL FOR SIMULATION OF POLYCRYSTALLINE MICROSTRUCTURES

In this section we address the construction of a statistical model for characterization and realization of 2D polycrystalline microstructures. The model can be seen as a computational tool for digitally simulating random microstructures in accordance with the available experimental data. This simulation tool will be employed in Section 3 to achieve a reasonable level of convergence in the identification of the probabilistic for mesoscale material description. Such simulations will also be used in Section 4 to generate model-based measurements for the validation of the probabilistic model.

2.1 Experimental Database

The data consist of microstructural-crystallographic measurements obtained from the electron backscatter diffraction (EBSD) technique [12, 13]. These maps provide direct information about the crystalline structures and the crystallographic orientations of the grains. The information obtained from EBSD maps can be used to study a variety of microstructural features such as orientation mapping, morphology and texture, phase identification, grain boundary, and defect. The processed data from this technique are also used to create the so-called orientation imaging micrograph [12], which enables a visual representation of crystallographic orientations. In this work, we use the measurements obtained from a rolled plate of aluminum alloy 2024-T351. Specimens were polished on a plane containing the rolling direction as well as the plane perpendicular to the rolling direction. The polished specimens were scanned using the EBSD technique and microstructural maps were obtained on each plane over the scanned area. More details about the experimental analysis can be found in [14]. In this research, only the data relative to the rolling plane are considered, which include three samples of approximately 12 mm$\times$1.5 mm microstructures. An experimental realization of the polycrystalline microstructure in the form of a microstructural map is shown in Fig. 1, where the colors indicate different grains with different orientations. Each EBSD map contains information on the geometry and the crystallography of approximately 4000 grains. On the basis of this information, in Sections 2.2 and 2.3 we construct a statistical model for characterization and simulation of 2D polycrystalline microstructures.

For characterization purposes, each grain $\mathcal{G}_i$ is represented by an equivalent ellipse $\mathcal{E}_i$ (the best ellipse fitting the grains). Thus, the geometry of a grain is characterized by the equivalent aspect ratio of the ellipse semiaxes, β. The crystallographic orientation of each grain is represented by a triplet of Euler angles [15], $(\theta_1, \theta_2, \theta_3)$, characterizing the relative orientation of the grain with respect to the polycrystal coordinate system. The marginal probability density

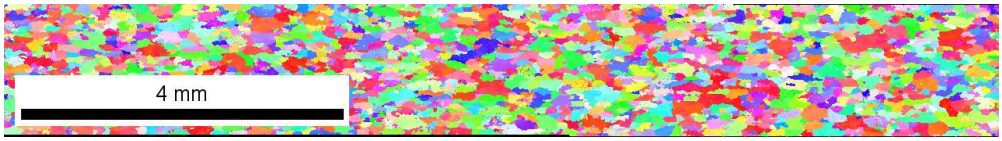

FIG. 1: Microstructural map of a samples of Al 2024-T351 obtained from the EBSD technique.

functions of the Euler angles and the equivalent aspect ratio, as estimated from experimental measurements, are plotted in Fig. 2 and 3, respectively. The angles θ_1 and θ_3 are, roughly speaking, uniformly distributed over $[0, 2\pi]$, while θ_2 has a slightly bimodal distribution supported over $[0, \pi/2]$. The distribution of the aspect ratio also has a slightly bimodal behavior where most of the realizations are significantly different from one. This implies that most of the grains are elongated. Furthermore, the statistics of major axis orientation of the fitting ellipses, also available

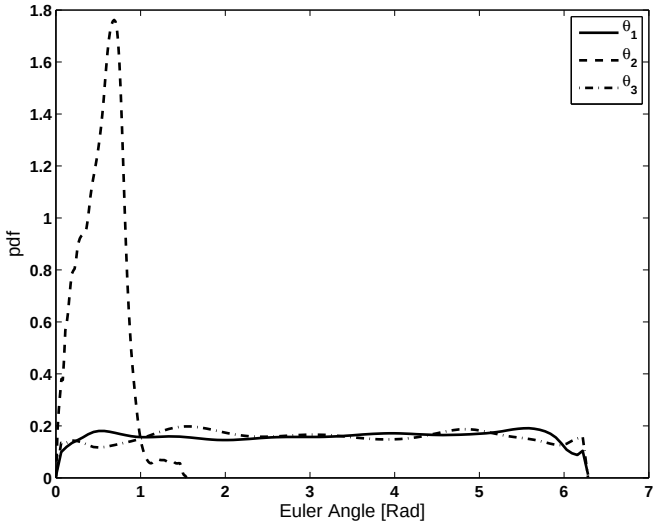

FIG. 2: Plot of the marginal probability density functions of Euler angles.

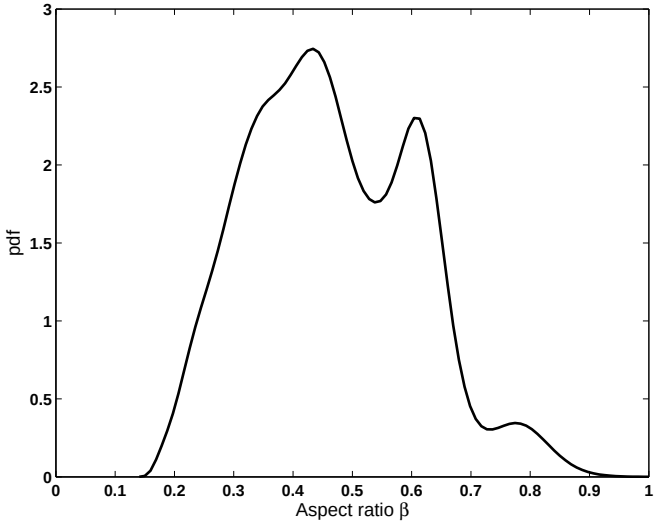

FIG. 3: Plot of the probability density function of β.

from EBSD data, implies that the grains are almost all elongated along the so-called rolling direction (the horizontal direction in Fig. 1).

2.2 Random Geometry

The first step in digitally generating a 2D microstructure in accordance with the experimental data involves the simulation of the random geometry. The Voronoi tessellation technique [16, 17] has been widely used in the mechanics and physics of random media as a simple model for a variety of material microstructures. It is particularly considered as a common model for a two-dimensional representation of polycrystalline microstructures in metallic alloys [18, 19]. For the polycrystalline materials, the tessellation is typically generated from a homogeneous Poisson process and is referred to as a Poisson Voronoi tessellation. The classical Voronoi tessellation is defined with respect to the Euclidean distance. The resulting partitioning technique is not capable of generating a microstructure with grains elongated in a given direction. However, as mentioned in Section 2.1, most of the grains in the type of alloy considered in this research are elongated along the rolling direction. This difficulty is resolved by making use of the so-called Voronoi-G tessellation introduced by Scheike [20] and briefly reviewed in this section. The Voronoi-G tessellation technique essentially relies on allowing the anisotropic growth of the Voronoi cells by replacing the Euclidean distance in the definition of classical Voronoi tessellation with a more general form. The resulting representation has a parameter for each dimension which controls the elongation of the cells in the desired direction. Let $\mathcal{D}$ be a bounded open set in d-dimensional Euclidean space, $\mathbb{R}^d$. Let $\{\mathbf{x}_{tes}^{(i)}\}_{i=1}^{N_\mathcal{G}}$ be the set of generating points belonging to the closure of $\mathcal{D}$. In the classical Voronoi tessellation, the cell $\mathcal{V}(\mathbf{x}_{tes}^{(i)})$ generated by $\mathbf{x}_{tes}^{(i)}$ is the set of all the points of $\mathcal{D}$ that are closer to $\mathbf{x}_{tes}^{(i)}$ than any other generating point, the closeness being defined with respect to the Euclidean distance in $\mathbb{R}^d$. As a consequence, the collection of all Voronoi cells $\{\mathcal{V}(\mathbf{x}_{tes}^{(i)})\}_{i=1}^{N_\mathcal{G}}$ partitions the space into disjoint space-filling regions. The set of closed convex polytopes obtained in this manner is then referred to as Voronoi tessellation (also known as Dirichlet tessellation or Dirichlet mosaics). A simple and efficient algorithm for generating the Voronoi tessellation of a set of points on a plane is presented in [21]. MATLAB users may find the functions `voronoi` and `voronoin` useful for simulation of 2D Voronoi tessellations. For $(\mathbf{x}, \mathbf{x'}) \in \mathbb{R}^d \times \mathbb{R}^d$, let $(\mathbf{x}, \mathbf{x'}) \mapsto d_G(\mathbf{x}, \mathbf{x'})$ be a generalized distance defined by

$$d_G(\mathbf{x}, \mathbf{x'}) = \sqrt{(\mathbf{x} - \mathbf{x'})^T \, [G] \, (\mathbf{x} - \mathbf{x'})}, \tag{1}$$

where superscript T represents the transpose operator and $[G]$ is a positive-definite symmetric matrix. The cell $\mathcal{V}_G(\mathbf{x}_{tes}^{(i)})$ of the Voronoi-G tessellation, generated by point $\mathbf{x}_{tes}^{(i)}$, is then defined as

$$\mathcal{V}(\mathbf{x}_{tes}^{(i)}) \stackrel{\text{def}}{=} \{\mathbf{x} \in \mathcal{D} \mid d_G(\mathbf{x}_{tes}^{(i)}, \mathbf{x}) \leq d_G(\mathbf{x}_{tes}^{(i)}, \mathbf{x}_{tes}^{(j)})\}, \tag{2}$$

in which $j = 1, ..., N_\mathcal{G}, j \neq i$. From the definition of distance in Eq. (1), it is obvious that by setting $[G] = [I_d]$, $[I_d]$ being the identity matrix, one can recover the classical Voronoi tessellation. It can be shown [20] that generating elongated cells in the horizontal direction can be performed by letting $[G]$ take the following form:

$$[G] = \begin{bmatrix} (1/s)^2 & 0 \\ 0 & 1 \end{bmatrix}, \tag{3}$$

in which $s \in \mathbb{R}_*^+ \subset \mathbb{R}^+$ is a positive real quantity. The parameter s characterizes the rate of growth of the cell in the horizontal direction and as such $(1/s)$ may be seen as the overall aspect ratio. Thus, having this parameter identified from the experimental distribution, one can digitally generate microstructures in which the equivalent aspect ratios of the grains are statistically consistent with the available data. Note that this technique does not allow control over the scaling of individual cells in the tessellation and as such may introduce a modeling bias in the numerical simulation. Here, we use the minimum relative entropy method to obtain an estimate $\hat{s}$ of s such that

$$\hat{s} = \underset{s \in \mathbb{R}^+}{\arg\min} \; D^{\mathrm{KL}} \left[\hat{p}_\beta(\beta) \parallel p_\beta(\beta|s) \right], \tag{4}$$

where $x \mapsto \hat{p}_\beta(x)$ and $x \mapsto p_\beta(x\,|s)$ are probability density functions of aspect ratio estimated, respectively, from experimental realizations (Fig. 3) and from the Monte Carlo simulation of the Voronoi-G microstructures for a given value of s and $D^{\mathrm{KL}}(\cdot \parallel \cdot)$ denotes the relative entropy (also known as Kullback-Leibler divergence) [22, 23], which is a positive-valued nonsymmetric distancelike measure of the difference between two probability distributions and is defined as

$$D^{\mathrm{KL}}\left[\hat{p}_\beta(\beta) \parallel p_\beta(\beta|s)\right] = \int_{\mathbb{R}^+} \hat{p}_\beta(\beta) \log \frac{\hat{p}_\beta(\beta)}{p_\beta(\beta|s)} d\beta. \tag{5}$$

The plot of the relative entropy as a function of s, shown in Fig. 4, indicates that the minimum is achieved for $\hat{s} = 2.0$.

The procedure for generating the elongated microstructure using the Voronoi-G tessellation technique is presented below [20]. Figure 5 shows two digitally simulated microstructures obtained from the same underlying Poisson point process before and after elongation.

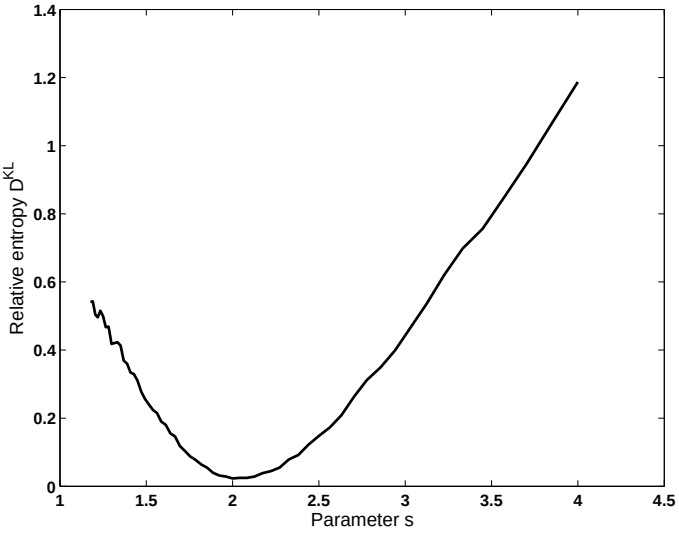

FIG. 4: Plot of the relative entropy function $s \mapsto D^{\mathrm{KL}}[\hat{p}_\beta(\beta) \parallel p_\beta(\beta|s)]$.

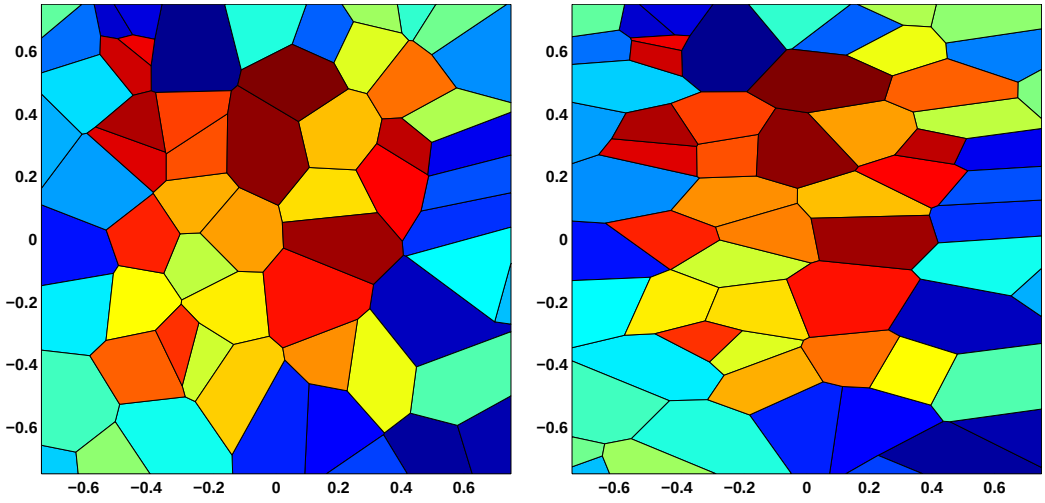

FIG. 5: Example of digitally simulated microstructure, without (left) and with (right) elongation.

Algorithm 1: Construction of the Voronoi-G tessellation.

$[Q] \leftarrow [G] = [Q]^T[Q]$;
populate the generating points $\mathbf{x}_{tes}^{(i)} \in \mathcal{D},\ i = 1, \ldots, N_{\mathcal{G}}$;
for $i \leftarrow 1, N_{\mathcal{G}}$ **do**
    $\tilde{\mathbf{x}} \leftarrow [Q]\mathbf{x}_{tes}^{(i)}$;
    compute the cell $\mathcal{V}(\tilde{\mathbf{x}}_{tes}^{(i)})$ generated by $\tilde{\mathbf{x}}_{tes}^{(i)}$;
    forall $\mathbf{y} \in \mathcal{V}(\tilde{\mathbf{x}}_{tes}^{(i)})$ **do**
        $\tilde{\tilde{\mathbf{y}}} \leftarrow [Q]^{-1}\mathbf{y}$;
    end
    define the Voronoi-G tessellation $\mathbf{y} \in \mathcal{V}_G(\hat{\mathbf{x}}_{tes}^{(i)}) \leftarrow \tilde{\tilde{\mathbf{y}}}$
end

2.3 Random Crystallographic Orientation

The next step in developing the statistical model of material microstructure is concerned with the characterization of random material properties from the available experimental data. In a polycrystalline microstructure, the elastic material properties are fully defined by prescribing single crystal elastic constants and a set of Euler angle triplets representing the crystallographic orientations of the grains with respect to the polycrystal reference frame. Since the elastic properties of a single grain are generally anisotropic, mismatches in the orientations of the grains lead to a changing set of elastic properties that is the major source of heterogeneity in the properties of polycrystalline materials. The language and methods of stochastic field theory, being capable of describing the spatial variation of complex patterns, seem to be a natural approach for the probabilistic representation of crystallographic orientation. As such, the present section addresses the construction of a random field model for spatially varying vector-valued Euler angles. The plot of estimated marginal probability densities in Fig. 2 clearly shows the non-Gaussian characteristics of random Euler angles. The characterization and simulation of non-Gaussian random processes have been extensively studied over the past few decades [24–28] and is still an area of active research. Since the higher order finite-dimensional distributions are often unavailable in practice, many existing simulation algorithms are based on matching prescribed marginal probability distribution functions and covariance function. A wide range of simulation approaches rely on the class of the so-called *translation processes* pioneered by Grigoriu [29, 30]. A translation process is essentially a non-Gaussian random process that can be represented by a memoryless transformation of an underlying Gaussian process. By postulating a translation form for the desired non-Gaussian process, a simulation can be performed by first generating a standard Gaussian process with an appropriate target covariance function, and then applying a memoryless transformation based on the prescribed marginal cumulative distribution functions (CDF). In general, it is not always guaranteed to find a translation form for any given choice of covariance function and non-Gaussian marginal distributions. From a theoretical point of view, the covariance function and the marginal distribution must satisfy certain compatibility conditions to ensure the existence of an associated translation process [25, 31]. Arwade and Grigoriu [19] modeled the Euler angles random field as a vector-valued translation field with prescribed marginal distributions and usual moment-product correlation function. In this case the moment-product correlation (also covariance) of the underlying standard Gaussian field is related to that of the non-Gaussian field implicitly in the form of an integral equation. The solution typically requires an iterative procedure and the integrals need to be evaluated numerically.

In this paper we circumvent the difficulties noted above by making use of the fractile correlation [32] instead of the usual moment-product correlation. The fractile correlation function, obtained from empirical observations, can be analytically related to the product-moment correlation of a Gaussian process. Given this correlation function, a Gaussian process can then be simulated and transformed using a CDF mapping to satisfy prescribed marginal distribution functions. In the following, we present the construction of such a correlation structure for the Euler angles random field from the available experimental measurements. We also present the simulation algorithm to generate the samples of the resulting random field.

2.3.1 Derivation of Random Field Model for Euler Angles

Let $(\mathbf{x},\gamma) \mapsto \mathbf{\Theta}(\mathbf{x},\gamma) = [\theta_1(\mathbf{x},\gamma), \theta_2(\mathbf{x},\gamma), \theta_3(\mathbf{x},\gamma)]$ be the $\mathbb{R}^3$-valued random field defined on a probability space $(\mathit{\Gamma}, \mathscr{F}, P)$, indexed by a bounded domain $\mathcal{D}$ in $\mathbb{R}^d$ (d being an integer, $1 \leq d \leq 3$), corresponding to the Euler angle representation of the crystallographic orientation field for a polycrystalline microstructure. For notational simplicity, hereafter the argument γ will be dropped unless needed for clarity. The spatial variation of the orientation field in second moment is characterized by a second-order tensor-valued covariance function $(\mathbf{x},\mathbf{x}') \mapsto [\Sigma^{\Theta}(\mathbf{x},\mathbf{x}')]$ defined for all $(\mathbf{x},\mathbf{x}')$ in $\mathbb{R}^d \times \mathbb{R}^d$ by

$$[\Sigma^{\Theta}(\mathbf{x},\mathbf{x}')] = \mathrm{E}\{[\mathbf{\Theta}(\mathbf{x}) - \underline{\Theta}(\mathbf{x})] \otimes [\mathbf{\Theta}(\mathbf{x}') - \underline{\Theta}(\mathbf{x}')]\}, \tag{6}$$

where $\mathrm{E}\{\cdot\}$ is the mathematical expectation, the symbol $\otimes$ is the tensor (or dyadic) product, and the underline denotes the mean value. Let us assume that the marginal distribution functions of $\mathbf{\Theta}(\mathbf{x})$ are invariant under translations. Denoting the associated marginal CDF as $F_i,\ i = 1,2,3$, we introduce a new $\mathbb{R}^3$-valued random field $\mathbf{x} \mapsto \mathbf{U}(\mathbf{x})$ such that its components, $\mathbf{u}_i$, are given by

$$\mathbf{u}_m(\mathbf{x}) = F_m[\theta_m(\mathbf{x})], \qquad m = 1,2,3. \tag{7}$$

The second-order tensor-valued fractile correlation function of $\mathbf{\Theta}(\mathbf{x})$, $(\mathbf{x},\mathbf{x}') \mapsto [\mathcal{R}(\mathbf{x},\mathbf{x}')]$ then reads

$$\begin{aligned}[\mathcal{R}(\mathbf{x},\mathbf{x}')]_{mn} &= \frac{\mathrm{E}\{[\mathbf{u}_m(\mathbf{x}) - \underline{u}_m(\mathbf{x})][\mathbf{u}_n(\mathbf{x}') - \underline{u}_n(\mathbf{x}')]\}}{\sqrt{\mathrm{E}\{[\mathbf{u}_m(\mathbf{x}) - \underline{u}_m(\mathbf{x})]^2\}\mathrm{E}\{[\mathbf{u}_n(\mathbf{x}') - \underline{u}_n(\mathbf{x}')]^2\}}} \\ &= 12\mathrm{E}\{\mathbf{u}_m(\mathbf{x})\mathbf{u}_n(\mathbf{x}')\} - 3.\end{aligned} \tag{8}$$

It is readily deduced from the definition that the fractile correlation is invariant with respect to monotonic transformations. Let us assume that a translation form for the random field $\mathbf{\Theta}(\mathbf{x})$ exists, that is $\mathbf{\Theta}(\mathbf{x})$ can be written as a transformation of a Gaussian field as follows:

$$\theta_m(\mathbf{x}) = F_m^{-1}\big(\Phi[\zeta_m(\mathbf{x})]\big), \qquad m = 1,2,3, \tag{9}$$

where $\zeta_m(\mathbf{x})$ is the zero-mean unit-variance component of an $\mathbb{R}^3$-valued Gaussian random field $\mathbf{x} \mapsto \boldsymbol{Z}(\mathbf{x}) = [\zeta_1(\mathbf{x}), \zeta_2(\mathbf{x}), \zeta_3(\mathbf{x})]$ and Φ is the CDF of a standard Gaussian variate. Applying the monotonic transformation of the form given by Eq. (7) to the both sides of Eq. (9) reads

$$F_m[\theta_i(\mathbf{x})] = \Phi[\zeta_m(\mathbf{x})] = \mathbf{u}_m(\mathbf{x}), \qquad m = 1,2,3, \tag{10}$$

which implies that the fractile correlations of the translation field $\mathbf{\Theta}(\mathbf{x})$ and its underlying Gaussian are matching. The moment-product correlation function (also covariance function) of the standard Gaussian field can be obtained from its fractile correlation using the following simple relationship, originally proposed by Pearson in 1904 for the case of random variables (see [33]):

$$[\Sigma(\mathbf{x},\mathbf{x}')]^Z_{mn} = 2\sin\left(\frac{\pi}{6}[\mathcal{R}(\mathbf{x},\mathbf{x}')]_{mn}\right), \qquad m,n = 1,2,3. \tag{11}$$

Note that Eq. (11) results in a valid covariance function only if it is non-negative definite. Once a valid covariance function is in hand, the simulation of Euler angles random field can be done by first generating the samples of underlying zero-mean Gaussian field $\boldsymbol{Z}(\mathbf{x})$ with a prescribed covariance function $[\Sigma(\mathbf{x},\mathbf{x}')]^Z$, and then applying the transformation given by Eq. (9). Representing the random field $\boldsymbol{Z}(\mathbf{x})$ in terms of its Karhunen-Loeve decomposition [34, 35] reads

$$\boldsymbol{Z}(\mathbf{x},\gamma) = \sum_{k=1}^{\infty} \sqrt{\lambda_k}\Psi_k(\mathbf{x})\xi_k(\gamma), \tag{12}$$

where $\{\xi_k(\gamma)\}$ is a set of uncorrelated standard Gaussian random variables, λ_k and $\Psi_k(\mathbf{x})$ are deterministic quantities representing, respectively, the eigenvalue and $\mathbb{R}^3$-valued eigenfunction of the covariance function $[\Sigma(\mathbf{x}, \mathbf{x'})]^Z$ such that its spectral decomposition reads

$$[\Sigma(\mathbf{x}, \mathbf{x}')]^Z = \sum_{k=1}^{\infty} \lambda_k \Psi_k(\mathbf{x}) \otimes \Psi_k(\mathbf{x'}). \tag{13}$$

In practice the Karhunen-Loeve expansion is truncated after a finite number of terms, M, leading to

$$\tilde{\boldsymbol{Z}}(\mathbf{x}, \gamma) = \sum_{k=1}^{M} \sqrt{\lambda_k} \Psi_k(\mathbf{x}) \xi_k(\gamma). \tag{14}$$

The covariance function associated with the truncated series then reads

$$[\Sigma(\mathbf{x}, \mathbf{x}')]^{\tilde{Z}} = \sum_{k=1}^{M} \lambda_k \Psi_k(\mathbf{x}) \otimes \Psi_k(\mathbf{x'}). \tag{15}$$

Once a realization of the Gaussian random field is generated from Eq. (14), the corresponding realization of the Euler angle field is obtained using the transformation given by Eq. (9).

2.3.2 Estimation of Correlation Structure

This section is concerned with the estimation of the correlation structure from the available experimental measurements of Euler angle triplets. Let $\mathcal{D}_{exp} \subset \mathbb{R}^2$ be the experimental domain of the microstructure for which the EBSD data were collected. Let $\{\mathbf{x}_{exp}^{(g)}\}_{g=1}^{N_{exp}} \in \mathcal{D}_{exp}$ be the set of points at which the crystallographic measurements were taken and $(\hat{\vartheta}_1^g, \hat{\vartheta}_2^g, \hat{\vartheta}_3^g)$ denotes the corresponding measurements of the vector of Euler angles. Let each grain be approximated by an equivalent ellipse $\mathcal{E}_g$ within which the Euler angles are considered to be constant. The information on equivalent ellipses is directly available from the output of the EBSD technique. The experimental field of Euler angles can be approximately represented as

$$\tilde{\vartheta}_m(\mathbf{x}) = \sum_{g=1}^{N_{exp}} \hat{\vartheta}_m^{(g)} \mathcal{I}^{(g)}(\mathbf{x}), \qquad m = 1, 2, 3, \tag{16}$$

where $\mathcal{I}^{(g)}(\mathbf{x}) : \mathbb{R}^d \mapsto \{0, 1\}$ denotes the indicator function associated with $\mathcal{E}_g$, that is

$$\mathcal{I}^{(g)}(\mathbf{x}) = \begin{cases} 1, & \text{if } \mathbf{x} \in \mathcal{E}_g, \\ 0, & \text{otherwise.} \end{cases} \tag{17}$$

The corresponding fractiles can be expressed as

$$\tilde{\mathbf{u}}_m(\mathbf{x}) = \sum_{g=1}^{N_{exp}} \hat{\mathbf{u}}_m^{(g)} \mathcal{I}^{(g)}(\mathbf{x}), \qquad m = 1, 2, 3, \tag{18}$$

in which, according to Eq. (7), $\hat{\mathbf{u}}_m^{(g)}$ is given by

$$\hat{\mathbf{u}}_m^{(g)} = \tilde{F}_m(\hat{\vartheta}_m^g), \tag{19}$$

where $\tilde{F}_m$ is the marginal CDF of Euler angles estimated from the available measurement.

For the sake of simplicity in estimation of correlation functions, we assume that the Euler angle random field is weakly homogeneous and isotropic, that is the second-order moment is invariant under any translation and rotation in

$\mathbb{R}^d$. Thus, the correlation function depends on only the distance $\eta = \|\mathbf{x} - \mathbf{x}'\|$ of two spatial points $(\mathbf{x}, \mathbf{x}')$. Making use of Eq. (8), an estimate of the fractile correlation function can be obtained as

$$[\tilde{\mathcal{R}}(\eta)]_{mn} = \frac{12}{N_k \times N_l} \sum_{k=1}^{N_k} \sum_{l=1}^{N_l} \tilde{\mathbf{u}}_m \left(\mathbf{x}_{exp}^{(k)}\right) \tilde{\mathbf{u}}_n \left(\mathbf{x}_{exp}^{(k)} + \eta \hat{\mathbf{n}}_l\right) - 3, \tag{20}$$

where $\{\hat{\mathbf{n}}_l\}_{l=1}^{N_l}$ is a finite set of distinct unit vectors and N_k is the number of measurement points $\mathbf{x}_{exp}^{(k)}$ for which $\mathbf{x}_{exp}^{(k)} + \eta \hat{\mathbf{n}}_l \in \mathcal{D}_{exp}$ for all $l = 1, \ldots, N_l$. Obviously, as the number N_l of unit vectors considered in the simulation increases, the accuracy in the estimation of the correlation function will increase. The plots of estimated fractile auto- and cross-correlation functions are shown in Fig. 6. It is seen that, roughly speaking, the second Euler angle θ_2 is not correlated with the other two. Also, comparing the correlation range with the average grain size indicates a short-range correlation among the neighboring grains. This suggests that for the particular material samples under study the Euler angles can be adequately modeled as spatially uncorrelated random vector. A similar observation has been reported by Arwade and Grigoriu [19] for aluminum alloy; however, they stated that other studies have indicated the possibility of encountering long-range correlation in orientation in aluminum polycrystals. As such, the general framework presented in this section for constructing a random field model for Euler angles is useful since it can incorporates the possible spatial correlation in the crystallographic orientation of the grains.

The plots of estimated fractile correlation functions, Fig. 6, suggest that an exponential form can be a suitable model for the fractile correlation of the Euler angles field. We postulate a correlation structure of the form $a_{mn} \exp(-\eta/l_{mn})$, where the parameters a_{mn} and l_{mn} are identified by fitting the exponential form to the estimated correlation functions. The plots of the best exponential fits to the estimated fractile correlations are shown in Fig. 7. The identified values of a_{mn} and l_{mn} for each case are reported on the plots. The exponential correlation function can be used for simulation of the Euler angle random field by setting $[\mathcal{R}(\eta)]_{mn} = a_{mn} \exp(-\eta/l_{mn})$ in Eq. (11), where $(\mathbf{x}, \mathbf{x}')$ is replaced by η.

2.3.3 Numerical Simulation of the Euler Angle Random Field

Let us consider the domain $\mathcal{D} \subset \mathbb{R}^2$ of a Voronoi-G polycrystal generated using the procedure in Section 2.2. Let $\{\mathbf{c}_i\}_{i=1}^{N_\mathcal{G}} \in \mathcal{D},\ i = 1, \ldots, N_\mathcal{G}$ be the set of geometric centroids of the grains $\{\mathcal{G}_i\}_{i=1}^{N_\mathcal{G}}$ in the generated polycrystal. Making use of the notation introduced in the previous section, the components of the orientation field $x \mapsto \boldsymbol{\Theta}(\mathbf{x}) = [\theta_1(\mathbf{x}), \theta_2(\mathbf{x}), \theta_3(\mathbf{x})]$ for the digitally generated microstructure can be represented as follows:

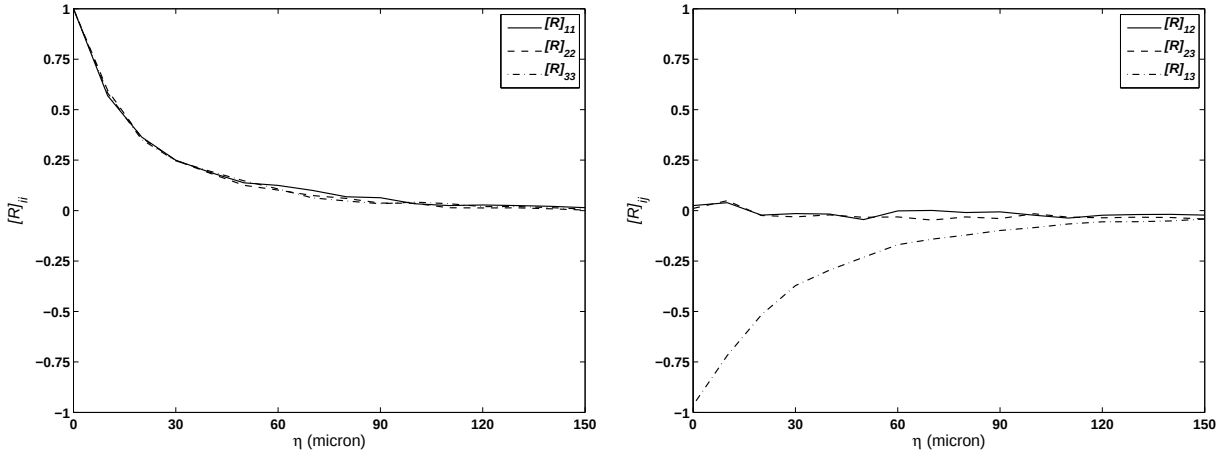

FIG. 6: The fractile auto- (left) and cross- (right) correlation functions as estimated from experimental data.

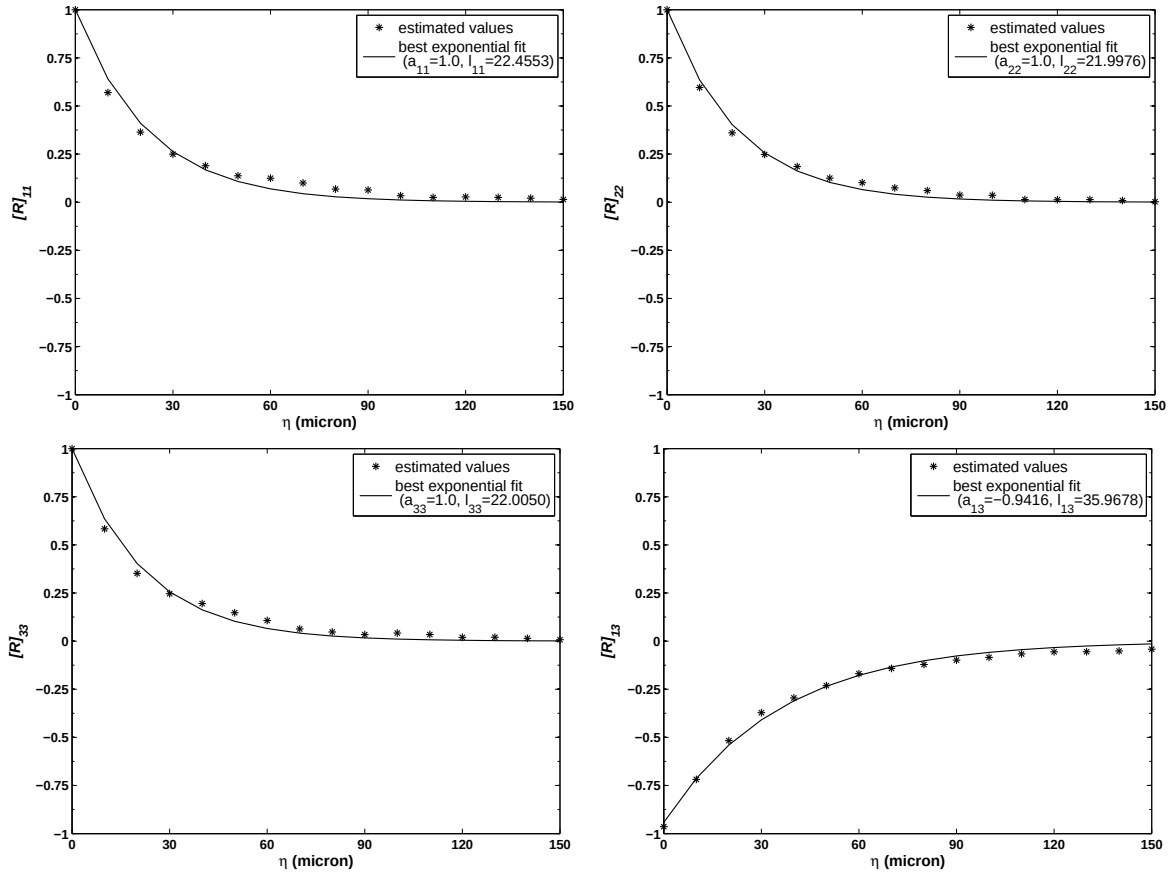

FIG. 7: Best exponential fits to the estimated fractile correlation functions.

$$\theta_m(\mathbf{x}) = \sum_{i=1}^{N_{\mathcal{G}}} \hat{\theta}_m^{(i)} \mathcal{I}^{(i)}(\mathbf{x}), \qquad m = 1, 2, 3, \tag{21}$$

where $\hat{\theta}_m^{(i)}$ is the component m of the triplet of Euler angles corresponding to the grain $\mathcal{G}_i$. Hence, the simulation of the orientation field will rely on generating the sample of Euler angle triplet at each center point $\mathbf{c}_i$. For implementation purposes, we introduce a vector-valued random variable $\widehat{\boldsymbol{\Theta}} = (\widehat{\Theta}_1, \ldots, \widehat{\Theta}_{3N_{\mathcal{G}}})$, the components of which are defined in the following fashion:

$$\widehat{\Theta}_{(i-1)\times 3+m} = \hat{\theta}_m^{(i)} \quad i = 1, \ldots, N_{\mathcal{G}}, \quad m = 1, 2, 3. \tag{22}$$

The second moment properties of $\widehat{\boldsymbol{\Theta}}$ are characterized by a $3N_{\mathcal{G}} \times 3N_{\mathcal{G}}$ fractile correlation matrix $[\widehat{\mathcal{R}}] = [[\mathcal{R}]^{ij}]$ where the submatrix $[\mathcal{R}]^{ij}$ is obtained making using of the correlation structure identified in Section 2.3.2 in the following manner:

$$[\mathcal{R}]^{ij}_{mn} = a_{mn} \exp(-\|\mathbf{c}_i - \mathbf{c}_j\|/l_{mn}), \quad i, j = 1, \ldots, N_{\mathcal{G}}, \quad m, n = 1, 2, 3. \tag{23}$$

From the constructed fractile correlation matrix $[\widehat{\mathcal{R}}]$, one can readily obtain the corresponding covariance matrix of the underlying Gaussian image using Eq. (6). The samples of Euler angles for each grain are then generated by employing the Karhunen-Loeve expansion technique and making use of the transformation given by Eq. (9), as described in Section 2.3.1. The numerical procedure for simulating the orientation field, given the geometry of a Voronoi-G polycrystal, is presented below.

Once an Euler angle triplet $\Theta^g = (\theta_1^g, \theta_2^g, \theta_3^g)$ is simulated for a grain g, the corresponding elasticity tensor $\mathbb{C}^g$ of the grain in the polycrystal reference frame can be readily computed form the single crystal elasticity tensor $\mathbb{C}^{(\mathrm{cr})}$

Algorithm 2: Simulation of the orientation field.

compute the set of grain centroids $\{\mathbf{c}_i\}_{i=1}^{N_\mathcal{G}}$;
for $i \leftarrow 1, N_\mathcal{G}$ **do**
  for $j \leftarrow i, N_\mathcal{G}$ **do**
    $[\widehat{\mathcal{R}}] = [[\mathcal{R}]_{mn}^{ij}] \leftarrow a_{mn} \exp(-\|\mathbf{c}_i - \mathbf{c}_j\|/l_{mn}), \quad m,n = 1,2,3;$
  end
end
$[\Sigma]_{IJ}^{\widehat{Z}} \leftarrow 2\sin((\pi/6)[\widehat{\mathcal{R}}]_{IJ}), \quad I,J = 1,\ldots,3N_\mathcal{G};$
compute the eigenvalues $\{\hat{\lambda}_k\}_{k=1}^{3N_\mathcal{G}}$ and eigenvectors $\{\hat{\Psi}_k\}_{k=1}^{3N_\mathcal{G}}$ of $[\Sigma]^{\widehat{Z}}$;
generate a set of statiscally independent standard Gaussian random variables $\{\xi_k\}_{k=1}^{N_\mathcal{G}}$;
$\widehat{\boldsymbol{Z}} = (\hat{\zeta}_1,\ldots,\hat{\zeta}_{3N_\mathcal{G}}) \leftarrow \sum_{k=1}^{3N_\mathcal{G}} \hat{\lambda}_k \hat{\Psi}_k \xi_k;$
for $m \leftarrow 1,3$ **do**
  for $i \leftarrow 1, N_\mathcal{G}$ **do**
    $\hat{\theta}_m^{(i)} \leftarrow F_m^{-1}\big(\Phi(\hat{\zeta}_{(i-1)\times 3+m})\big);$
  end
  $\theta_m(\mathbf{x}) \leftarrow \sum_{i=1}^{N_\mathcal{G}} \hat{\theta}_m^{(i)} \mathcal{I}^{(i)}(\mathbf{x});$
end
$\boldsymbol{\Theta}(\mathbf{x}) \leftarrow [\theta_1(\mathbf{x}), \theta_2(\mathbf{x}), \theta_3(\mathbf{x})];$

using the following tensorial transformation:

$$\mathbb{C}^g_{i'j'k'l'} = [R(\Theta^g)]_{i'i}[R(\Theta^g)]_{j'j}[R(\Theta^g)]_{k'k}[R(\Theta^g)]_{l'l}\mathbb{C}^{(\mathrm{cr})}_{ijkl}, \tag{24}$$

where the transformation matrix $[R(\Theta)]$ is given by

$$[R(\Theta)] = \begin{bmatrix} \cos\theta_1 & -\sin\theta_1 & 0 \\ \sin\theta_1 & \cos\theta_1 & 0 \\ 0 & 0 & 1 \end{bmatrix} \begin{bmatrix} 1 & 0 & 0 \\ 0 & \cos\theta_2 & -\sin\theta_2 \\ 0 & \sin\theta_2 & \cos\theta_2 \end{bmatrix} \begin{bmatrix} \cos\theta_3 & -\sin\theta_3 & 0 \\ \sin\theta_3 & \cos\theta_3 & 0 \\ 0 & 0 & 1 \end{bmatrix}. \tag{25}$$

In the case of aluminum, the single crystal has a cubic crystalline structure where $\mathbb{C}^{(\mathrm{cr})}$ takes the following form:

$$\mathbb{C}^{(\mathrm{cr})} = \begin{bmatrix} c_{11} & c_{12} & c_{12} & 0 & 0 & 0 \\ c_{12} & c_{11} & c_{12} & 0 & 0 & 0 \\ c_{12} & c_{12} & c_{11} & 0 & 0 & 0 \\ 0 & 0 & 0 & c_{44} & 0 & 0 \\ 0 & 0 & 0 & 0 & c_{44} & 0 \\ 0 & 0 & 0 & 0 & 0 & c_{44} \end{bmatrix}, \tag{26}$$

in which the single crystal elastic constants of aluminum are given by $c_{11} = 108$, $c_{12} = 61.3$ and $c_{44} = 28.5$, where the units are in gigapascals.

3. PROBABILISTIC MODEL FOR MESOSCALE ELASTICITY TENSOR

In this section we recall the construction of a probabilistic model for the mesoscale elastic behavior of materials with microstructures. The linear elastic constitutive matrix of this model is described mathematically as a bounded matrix-valued random variable. The probability model is established within the framework of the so-called *nonparametric approach for uncertainties* pioneered by Soize [9, 10, 36]. Having recourse to the MaxEnt principle and making use of the random matrix theory, this approach allows one to construct a probability measure of the random system

matrices without explicitly considering random parameters that could describe the mechanical behavior of the system or characterize the morphological features of the material. Based on this framework, Soize [37] introduced a class of positive-definite matrix-valued random field to model the three-dimensional linear elasticity tensor of a random, nonhomogeneous anisotropic material. The resulting probability model is characterized by a matrix-valued mean function and a set of scalar parameters controlling the spatial correlation lengths and the level of statistical fluctuations. Such a parametrization may facilitate experimental identification using an inverse problem scheme. This probability model was extended later [38] to construct a mesoscale probabilistic description of anisotropic heterogeneous material with microstructure. Within this framework, a model was derived [39] for bounded random matrices that are symmetric and positive-definite. The bounds are defined based on the concept of energy-based constraints on elasticity tensors introduced by Huet [8]. The resulting probability model can be useful to characterize the continuum elasticity matrix associated with the overall properties of heterogeneous materials that are bounded from below and above. These bounds are consistent with the theory of elasticity and implicitly reflect the variability in the material heterogeneity. A different formulation is recently proposed [11] to account for the boundedness constraints. The proposed approach invokes the class of random field previously introduced by Soize [38] and facilitates the extension of bounded random system matrices to the case of random fields. In this work we make use of this alternative formulation to model the mesoscale linear elastic constitutive matrix of a polycrystalline material as a bounded random matrix. The construction of the model is briefly reviewed in the present section.

3.1 Micromechanics-Based Bounds for the Mesoscale Properties of Linear Elastic Microstructure

We consider the domain of a random heterogeneous medium $\mathcal{D} \in \mathbb{R}^3$ with boundary $\partial\mathcal{D}$. The effective elasticity matrix $[C^{\text{eff}}]$ is obtained using the classical concept of RVE [2]. However, our special interest in this work is focused on the case where $\mathcal{D}$ is smaller than the RVE. The volume element $\mathcal{D}$ is thus a statistical volume element. Following the terminology introduced by Huet [8], the overall mechanical properties of a material in this scale are referred to as *apparent properties* and are random in nature. The relation between the effective and apparent properties was first examined by Huet by introducing the so-called partition theorem [8]. As the result, the inequalities between the effective and apparent elasticity tensors were established and the procedure to obtain the hierarchies of mesoscale bounds for the elastic properties was presented (see also [18] for a general review). The partition theorem essentially states that the effective properties of heterogeneous elastic bodies are bounded from below and above by the apparent properties obtained from applying two essential forms of boundary conditions to the any set of uniform partition of the associated RVE. The first case of the boundary condition is referred to as kinematic uniform boundary condition (KUBC) and corresponds to a prescribed displacement field $\mathbf{v}(\mathbf{x})$ applied to the boundary $\partial\mathcal{D}$ in the following form:

$$\mathbf{v}(\mathbf{x}) = \epsilon_0 \mathbf{x}, \quad \forall\, \mathbf{x} \in\ \partial\mathcal{D}. \tag{27}$$

In Eq. (27), ϵ_0 is the vector representation of a given symmetric second-order strain tensor. The associated kinematic apparent elasticity tensor $[\mathbf{C}_\epsilon^{\text{app}}]$ is defined such that

$$\langle \sigma \rangle = [\mathbf{C}_\epsilon^{\text{app}}]\langle \epsilon \rangle = [\mathbf{C}_\epsilon^{\text{app}}]\epsilon_0, \tag{28}$$

where $\langle \cdot \rangle$ represents the volume average over $\mathcal{D}$, that is,

$$\langle \sigma \rangle = \frac{1}{|\mathcal{D}|} \int_{\mathcal{D}} \sigma(\mathbf{x}) d\mathbf{x} \tag{29}$$

$$\langle \epsilon \rangle = \frac{1}{|\mathcal{D}|} \int_{\mathcal{D}} \epsilon(\mathbf{x}) d\mathbf{x}. \tag{30}$$

The second case of boundary condition is referred to as the static uniform boundary condition (SUBC) and corresponds to a prescribed traction vector field of the form

$$\mathbf{t}(\mathbf{x}) = \sigma_0 \mathbf{n}(\mathbf{x}), \quad \forall\, \mathbf{x} \in\ \partial\mathcal{D}, \tag{31}$$

where σ_0 is the vector representation of a given symmetric second-order stress tensor and $\mathbf{n}(\mathbf{x})$ is the unit vector normal to $\partial\mathcal{D}$ at $\mathbf{x}$. In this case, one can define the static apparent compliance tensor $[\mathbf{S}_\sigma^{\text{app}}]$, analogous to Eq. (28), such that

$$\langle\epsilon\rangle = [\mathbf{S}_\sigma^{\text{app}}]\langle\sigma\rangle = [\mathbf{S}_\sigma^{\text{app}}]\sigma_0. \tag{32}$$

Thus, the associated static apparent elasticity tensor, $[C_\sigma^{\text{app}}]$, reads

$$[C_\sigma^{\text{app}}] = [S_\sigma^{\text{app}}]^{-1}. \tag{33}$$

Now let us consider the set of n uniform partitions of $\mathcal{D}$ that is equal to or larger than the RVE. Let us denote these partitions as V_i, $i = 1, \ldots, n$. Applying KUBC and SUBC to each subdomain V_i yields a different pair of realizations of the kinematic and static apparent modulus matrices denoted as $[\mathbf{C}_\sigma^{\text{app}}(V_i)]$ and $[\mathbf{S}_\sigma^{\text{app}}(V_i)]$, respectively. Based on the partition theorem, the effective elastic matrix is bounded from below and above with the statistical average of these matrices, that is

$$[\widehat{\mathbf{C}}_\sigma^{\text{app}}] \leq [C^{\text{eff}}] \leq [\widehat{\mathbf{C}}_\epsilon^{\text{app}}], \tag{34}$$

where

$$[\widehat{\mathbf{C}}_\sigma^{\text{app}}] = \left\{\frac{1}{n}\sum_{i=1}^{n}[\mathbf{S}_\sigma^{\text{app}}(V_i)]\right\}^{-1}, \tag{35}$$

$$[\widehat{\mathbf{C}}_\epsilon^{\text{app}}] = \frac{1}{n}\sum_{i=1}^{n}[\mathbf{C}_\epsilon^{\text{app}}(V_i)]. \tag{36}$$

For the domain smaller than the RVE, invoking the partition theorem leads to hierarchical inequalities among the apparent tensor at various mesoscales [8]. For any given realization of the SVE, it can be shown that

$$[\widehat{\mathbf{C}}_\sigma^{\text{app}}] \leq [\mathbf{C}_\sigma^{\text{app}}] \leq [\mathbf{C}_m^{\text{app}}] \leq [\mathbf{C}_\epsilon^{\text{app}}] \leq [\widehat{\mathbf{C}}_\epsilon^{\text{app}}], \tag{37}$$

where $[\mathbf{C}_m^{\text{app}}]$ are the apparent elastic properties resulting from applying the so-called mixed boundary condition (MBC) on the volume element and, as such, are referred to as mixed apparent elasticity tensor. A special form of MBC is known as orthogonal uniform mixed boundary conditions [40]. This form includes the case of uniform uniaxial tension, which is of particular importance from an experimental point of view.

3.2 Overview of Model Construction

Let $\mathbb{M}_n^s$ be the set of all the $(n \times n)$ real symmetric matrices and $\mathbb{M}_n^+ \subset \mathbb{M}_n^s$ denotes the set of symmetric positive-definite matrices. Let $[\mathbf{C}] \in \mathbb{M}_n^+$ be the matrix representation of the fourth-order random apparent elasticity tensor of $\mathcal{D}$. Invoking the principles of minimum complementary energy and minimum potential energy, one can obtain two deterministic matrices $[C_l] \in \mathbb{M}_n^+$ and $[C_u] \in \mathbb{M}_n^+$ such that the following inequalities hold almost surely:

$$[0] < [C_l] < [\mathbf{C}] < [C_u], \tag{38}$$

where $[0]$ is the zero matrix. Note that the above inequalities are inferred in the positive-definite sense, i.e., $[X] > [Y]$ implies that $[X] - [Y]$ is a positive-definite matrix. Let Ω be the set of all the $n \times n$ real symmetric positive-definite matrices for which the inequalities (38) hold in the strict sense, that is $\Omega = \{[C] \in \mathbb{M}_n^+(\mathbb{R}) | [C_l] < [C] < [C_u]\}$. We denote the probability space on which Ω is defined by $(\Omega, \mathcal{T}, \mathcal{P})$, where $\mathcal{T}$ is the σ-algebra of subsets of Ω and $\mathcal{P}$ represents the probability measure on $\mathcal{T}$. Let us assume that $\mathcal{P}$ admits a probability density function $[C] \mapsto p_{[\mathbf{C}]}([C])$ from Ω into $\mathbb{R}^+ =]0, \infty[$. The probability distribution of $[\mathbf{C}]$ is then defined by $P_{[\mathbf{C}]} = p_{[\mathbf{C}]}([C])dC$, in which the measure dC on $\mathbb{M}_n^s(\mathbb{R})$ is given by

$$dC = 2^{n(n-1)/4} \prod_{1 \leq i \leq j \leq n} d[C]_{ij}, \tag{39}$$

where $d[C]_{ij}$ is the Lebesgue measure on $\mathbb{R}$ [9].

The generalization of the measure of entropy, introduced initially by Shanon [41] for discrete probability distributions, to the case of probability density function p reads

$$\mathrm{S}(p) = -\int_{\mathbb{M}_n^+(\mathbb{R})} p([X]) \ln(p([X]))dX. \tag{40}$$

An estimation of $p_{[\mathbf{C}]}$ can be classically obtained having recourse to the maximum entropy (MaxEnt) principle presented by Jaynes [42, 43] in the case of random vectors. The MaxEnt principle consists of maximizing the measure of information entropy $S(p)$ under a set of constraints encompassing the available information. Using this principle, one can explicitly construct a probabilistic model using the available information and avoiding any bias on the estimation of the probability distribution due to the use of any additional information. Thus, the general expression for the construction of the probability density function $p_{[\mathbf{C}]}$ using the MaxEnt principle is stated as

$$p_{[\mathbf{C}]} = \underset{p \in \mathcal{P}_{ad}}{\arg} \max \mathrm{S}(p), \tag{41}$$

where $\mathcal{P}_{ad}$ denotes the set of all the admissible probability density functions, with support Ω, fulfilling all the constraints associated with the available information. The choice of uniform measure in the MaxEnt principle as stated and used in this paper is merely arbitrary. In other words, we presume, without justification, that our state of indifference is described by a uniform measure. A study of this point in connection with multiscale simulation and experimentation capabilities would be of great interest, but falls outside the realm of this paper.

Based on the general framework explained above, two probabilistic models for deterministically bounded positive-definite matrix-valued random variable were recently derived [11, 39]. The major difference in the construction of these two models is in the way that the boundedness constraint is introduced. In the probabilistic model derived in [39] the constrains associated with the lower and upper bounds are directly enforced on the random matrix $[\mathbf{C}]$. The final form of the probability density function $[C] \mapsto p_{[\mathbf{C}]}([C])$ is explicitly constructed. In this case the probability density function takes the form of a generalized matrix variate Kummer-Beta distribution [44]. Alternatively, the boundedness constraints can be implicitly implemented through a suitable transformation on $[\mathbf{C}]$ [11]. We use this formulation, which relies on introducing the shifted inverse random matrix $[\mathbf{N}]$ defined by

$$[\mathbf{N}] = ([\mathbf{C}] - [C_l])^{-1} - ([C_u] - [C_l])^{-1}. \tag{42}$$

The condition of $([\mathbf{C}] - [C_l])^{-1} \in \mathbb{M}_n^+$, respectively, $([C_u] - [\mathbf{C}])^{-1} \in \mathbb{M}_n^+$, is readily deduced from the symmetric positive-definiteness of the random matrix $[\mathbf{C}] - [C_l]$, respectively, $[C_u] - [\mathbf{C}]$. Consequently, $[\mathbf{N}]$ is also symmetric positive-definite, that is, $[\mathbf{N}] \in \mathbb{M}_n^+(\mathbb{R})$. Let us assume that the matrix-valued random variable $[\mathbf{N}]$ admits a probability density function $[N] \mapsto p_{[\mathbf{N}]}([N])$ defined on $\mathbb{M}_n^+$. Using the MaxEnt principle, $p_{[\mathbf{N}]}$ can be constructed by solving the following optimization problem:

$$\begin{aligned} &\text{minimize } [-S(p_{[\mathbf{N}]})] \\ &\text{subject to} \end{aligned} \tag{43}$$

$$\int_{\mathbb{M}_n^+(\mathbb{R})} p_{[\mathbf{N}]}([N])dN = 1, \tag{44}$$

$$\int_{\mathbb{M}_n^+(\mathbb{R})} [N] p_{[\mathbf{N}]}([N])dN = [\underline{N}] \in \mathbb{M}_n^+(\mathbb{R}), \tag{45}$$

$$\int_{\mathbb{M}_n^+(\mathbb{R})} \ln\{\det([N])\}\, p_{[\mathbf{N}]}([N])dN = c_N,\ |c_N| < +\infty, \tag{46}$$

It is readily seen that $[\mathbf{N}]$ belongs to the class of positive-definite matrix-valued random variable presented in [9]. The constraint in Eqs. (45) and (46) define the available information. The constraint in Eq. (45) implies that the mean value of $[\mathbf{N}]$ is given by the $\mathbb{M}_n^+$-valued matrix $[\underline{N}]$, while Eq. (46) ensures the existence of the moments associated with the inverse random matrix $[\mathbf{N}]^{-1}$ (see [9] for the proof). The above optimization problem is classically solved by the

method of Lagrange multipliers. Let $\lambda_0 \in \mathbb{R}$, $[\Lambda_{[\mathbf{N}]}] \in \mathbb{M}_n^+(\mathbb{R})$ and $\lambda \in \mathbb{R}$ be the Lagrange multipliers associated with Eqs. (44), (45), and (46), respectively. The resulting probability density function $[N] \mapsto p_{[\mathbf{N}]}([N])$ takes the form [9]

$$p_{[\mathbf{N}]} = \mathbb{I}_{\mathbb{M}_n^+(\mathbb{R})}([N]) c_0 \det([N])^{\lambda-1} \text{etr}\{-[\Lambda_{[\mathbf{N}]}][N]\}, \tag{47}$$

where $\text{etr}\{[X]\} = \exp\{\text{tr}([X])\}$, $c_0 = \exp(-\lambda_0 - 1)$ and $[X] \mapsto \mathbb{I}_{\mathbb{M}_n^+(\mathbb{R})}([X])$ is the indicator function for the set $\mathbb{M}_n^+(\mathbb{R})$, that is, $\mathbb{I}_{\mathbb{M}_n^+(\mathbb{R})}([X])$ is equal to 1 if $[X] \in \mathbb{M}_n^+(\mathbb{R})$ and 0 otherwise. For positive integer values of λ, Eq. (47) corresponds to the probability density function of a Wishart distribution [44]. Let $\delta_{[\mathbf{N}]}$ denote the dispersion parameter that controls the level of statistical fluctuation of the random matrix $[\mathbf{N}]$ defined as

$$\delta_{[\mathbf{N}]} = \left\{ \frac{E\{\|[\mathbf{N}] - [\underline{N}]\|_F^2\}}{\|[\underline{N}]\|_F^2} \right\}^{1/2}, \tag{48}$$

where $\|[X]\|_F = (\text{tr}\{[X][X]^*\})^{(1/2)}$ is the Frobenius norm. It has been shown that the quantities $\delta_{[\mathbf{N}]}$, λ and $[\Lambda_{[\mathbf{N}]}]$ are related through the following relationships [9]:

$$\delta_{[\mathbf{N}]} = \left\{ \frac{1}{n-1+2\lambda} \left(1 + \frac{(\text{tr}[\underline{N}])^2}{\text{tr}([\underline{N}]^2)} \right) \right\}^{1/2}, \tag{49}$$

$$[\Lambda_{[\mathbf{N}]}] = \frac{n-1+2\lambda}{2} [\underline{N}]^{-1}. \tag{50}$$

The generation of realizations of random matrix $[\mathbf{N}]$ with respect to Eq. (47) involves sampling from Gaussian and gamma univariate distributions. A numerical algorithm is proposed in [9] for this purpose and shall not be repeated here for the sake of brevity. Once the samples of $[\mathbf{N}]$ are generated, the corresponding realizations of the random matrix $[\mathbf{C}]$ is readily obtained from Eq. (42).

3.3 Calibration of the Probabilistic Model

This section is concerned with the calibration of the probabilistic model for random matrix $[\mathbf{N}]$ introduced in Section 3.2. The calibration task involves identification of the mean matrix $[\underline{N}]$ and the dispersion parameter $\delta_{[\mathbf{N}]}$ for a given mesoscopic domain of heterogeneous material. To that end, first the realizations of the apparent elasticity matrix $[\mathbf{C}]$ as well as the lower bound $[C_l]$ and upper bounds $[C_u]$ need to be computed. These quantities will in turn be used in Eq. (42) to compute the realizations of random matrix $[\mathbf{N}]$ from which $[\underline{N}]$ and $\delta_{[\mathbf{N}]}$ will be estimated. The details of numerical procedure for computing the realizations of the apparent tensors are presented elsewhere (see [11, Section 4.3.1]) and will not be detailed here for the sake of brevity. This procedure can be summarized as follows:

Step 0: Generate a realization of the 2D polycrystalline microstructure.

Step 1: Compute the realizations of $[\widehat{\mathbf{C}}_\epsilon^{\text{app}}]$ and $[\widehat{\mathbf{C}}_\sigma^{\text{app}}]$ by invoking the Huet's partition theorem [Eqs. (29) and (30)].

Step 2: Compute the realizations of $[\mathbf{C}_\epsilon^{\text{app}}]$ and $[\mathbf{C}_\sigma^{\text{app}}]$ by applying KUBC and SUBC, respectively.

Step 3: Compute the realization of the apparent elasticity matrix $[\mathbf{C}_m^{\text{app}}]$ by applying MBC (tension test for instance) and solving the following optimization problem:

$$[C_m^{\text{app}}] = \underset{[C_l]<[C]<[C_u]}{\arg\min} \|\langle \sigma \rangle_{MBC} - [C]\langle \epsilon \rangle_{MBC}\|. \tag{51}$$

The calculation of the apparent elasticity matrix in step 3 requires the estimation of an appropriate pair of deterministic bounds $[C_l]$ and $[C_u]$ extracted from the stochastic ones $[\mathbf{C}_\sigma^{\text{app}}]$ and $[\mathbf{C}_\epsilon^{\text{app}}]$. We use the deterministic bounds proposed in [11, 45] where $[C_l]$ and $[C_u]$ are defined as

$$[C_l] = \underset{[C]\in\mathcal{C}_l}{\arg\min} \sum_{k=1}^{N_{sim}} \|[C_\sigma^{\text{app}}(\omega_k)] - [C]\|_F, \tag{52}$$

$$[C_u] = \underset{[C]\in\mathcal{C}_u}{\arg\min} \sum_{k=1}^{N_{sim}} \|[C] - [C_\epsilon^{\text{app}}(\omega_k)]\|_F, \tag{53}$$

in which the argument $\omega_k,\ k = 1, ..., N_{sim}$ indexes the random realizations and the sets $\mathcal{C}_l$ and $\mathcal{C}_u$ are defined as

$$\mathcal{C}_l = \{[C] \in \mathbb{M}_n^+(\mathbb{R}) \mid [C] < [C_\sigma^{\text{app}}(\omega_k)], k = 1, \ldots, N_{sim}\}, \tag{54}$$

$$\mathcal{C}_u = \{[C] \in \mathbb{M}_n^+(\mathbb{R}) \mid [C_\epsilon^{\text{app}}(\omega_k)] < [C], k = 1, \ldots, N_{sim}\}. \tag{55}$$

For the purpose of calibration, we consider $N_{sim} = 100$ realizations of 0.3 mm×0.3 mm domain of microstructure of aluminum polycrystal generated using the procedure detailed in Section 2. Following the aforementioned procedure, the estimates of the lower and upper bounds are found to be

$$[\widetilde{C}_l] = 10^5 \begin{bmatrix} 1.0869 & 0.6068 & 0.0007 \\ 0.6068 & 1.0884 & 0.0007 \\ 0.0007 & 0.0007 & 0.2347 \end{bmatrix}, \tag{56}$$

$$[\widetilde{C}_u] = 10^5 \begin{bmatrix} 1.1487 & 0.5787 & 0.0013 \\ 0.5787 & 1.1477 & -0.0003 \\ 0.0013 & -0.0003 & 0.2825 \end{bmatrix}, \tag{57}$$

where the units are in megapascals. These estimated bounds, along with the realizations of the apparent elasticity tensor $[\mathbf{C}^{\text{app}}]$, obtained from Eq. (51), allow the corresponding realizations $[N(\omega_1)], ..., [N(\omega_{N_{sim}})]$ of $[\mathbf{N}]$ to be computed from Eq. (42). Finally, estimates of parameters $[\underline{N}]$ and $\delta_{\mathbf{N}}$ of the probabilistic model, can be readily determined as follows:

$$[\widetilde{\underline{N}}] = \frac{1}{N_{sim}} \sum_{k=1}^{N_{sim}} [N(\omega_k)], \tag{58}$$

$$\widetilde{\delta}_{\mathbf{N}} = \left\{ \frac{1}{N_{sim}\|[\widetilde{\underline{N}}]\|_F^2} \sum_{k=1}^{N_{sim}} \|[N(\omega_k)] - [\widetilde{\underline{N}}]\|_F^2 \right\}^{1/2}. \tag{59}$$

These parameters are found to be

$$\widetilde{\delta}_{\mathbf{N}} = 0.66, \tag{60}$$

and

$$[\widetilde{\underline{N}}] = 10^{-3} \begin{bmatrix} 0.2667 & 0.0879 & -0.0189 \\ 0.0879 & 0.2214 & 0.0277 \\ -0.0189 & 0.0277 & 0.2366 \end{bmatrix}. \tag{61}$$

Making use of the above parameters, the numerical Monte Carlo simulations are performed to sample the realizations of the random matrix $[\mathbf{N}]$ and subsequently the corresponding realizations of $[\mathbf{C}]$ can be readily computed. From the simulated realizations of $[\mathbf{C}]$, the dispersion parameter is estimated to be $\widetilde{\delta}_{[\mathbf{C}]}^{sim} = 0.009$. This small amount of statistical fluctuations can be related to weak anisotropy of aluminum single crystal [11].

4. VALIDATION

In Section 2 we presented the construction of a statistical model for characterization and realization of 2D polycrystals from the microstructural measurements extracted from EBSD maps. The resulting realizations of the microstructures were used in Section 3 to achieve a reasonable level of convergence in the identification of a probabilistic model for the mesoscale elasticity tensor of a polycrystalline material. Before utilizing this stochastic mechanistic model as a predictive tool for system level response, the confidence in the credibility of the model must be established by evaluating the quality of agreement between the predictions of the model and the experimental or model-based observations.

Models are often constructed on the basis of certain assumptions and simplifications and they are not more than an approximation of reality. Thus, from a conceptual point of view all models are wrong, but can be useful if their validity, within a specified confidence range, is ascertained. Having this in mind, the question of the validation is not the truth of the model from a physical point of view, but rather the adequacy of the model in representing a certain behavior in order to be used in predicting a desired response quantity. Hence, in the context of computational mechanics the validation task is stated from the perspective of intended uses of the model and the evaluation is performed with respect to a specific quantity of interest (QOI). In stochastic computational modeling, where the uncertainty is involved in either or both prediction and the observation data, a model validation has to properly accommodate these uncertainties. In this situation the validation task is often exercised on the basis of some error statistics (see [46–48] for instance).

In the following sections we will address the validation of the probabilistic model for the mesoscale elasticity tensor presented in Section 3.

4.1 Verifying the Calibration Process

As the most basic sense of validation, first we explore the level of confidence in the model performance when it is used to reproduce the observations that are directly related to, and at the same scale as, the physical quantity described by the model. In particular, as the quantities of interest, we consider the following scalar-valued random variables associated with the invariants of the apparent elasticity matrix $[\mathbf{C}]$:

$$\mathbf{J}_1 = \text{tr}([\mathbf{C}]), \tag{62}$$

$$\mathbf{J}_2 = \frac{1}{2}([\mathbf{C}]_{ii}[\mathbf{C}]_{jj} - [\mathbf{C}]_{ij}[\mathbf{C}]_{ji}), \tag{63}$$

$$\mathbf{J}_3 = \det([\mathbf{C}]), \tag{64}$$

where the Einstein index notation is employed in Eq. (63). The probability density functions (pdf's) of these quantities can be estimated making use of the samples of apparent elasticity matrix generated from the calibrated probabilistic model. These pdf's can also be estimated by performing fine scale simulation on realizations of random microstructures. By comparing these two set of pdf's, we can explore the performance of the mesoscale probabilistic model in reproducing the observable physical quantities. From a practical standpoint, such a probabilistic description for observations are often not available. Nevertheless, the comparison of these statistics can provide transparent measures to characterize the performance, which can be linked to the practical setting by hypothesis test.

For the purpose of validation, $N_{sim} = 500$ samples of the random matrix $[\mathbf{C}]$ are obtained from performing numerical Monte Carlo simulations using the probabilistic model of the mesoscale elasticity tensor. Moreover, N_{sim} realizations of 0.3 mm$\times$0.3 mm 2D microstructure are generated making use of the statistical model for polycrystalline microstructures developed in Section 2. Note that this is the same size of the SVE for which the model is calibrated. The corresponding realization of the apparent elasticity matrix for each microstructure is computed by performing a fine scale simulation following step 3 of the calibration procedure in Section 3.3 and making use of the deterministic bounds given by Eqs. (56) and (57). From these two sets of realizations, the corresponding set of values for $\mathbf{J}_1$, $\mathbf{J}_2$, and $\mathbf{J}_3$ are then computed. These values are in turn used to estimate the associated pdf's for model-based samples as well as fine scale simulations. The estimated pdf's are compared in Figs. 8–10. The results show that in all the cases more than 96% of the observations fall in these confidence intervals. This reflects a relatively high level of confidence in the performance of the model. The computed values of the mean and coefficient of variations (cov) for each case are reported in Table 1 for the sake of comparison.

As the next logical step, in the following sections we will study the model validation from the perspective of intended uses of the model. We will particularly explore the performance of the model in propagating the uncertainty from the fine scale to the coarse scale response. In other words, we will examine whether the variability in the predictions of the model with respect to a specific response quantity of interest (QOI) is consistent with the fine scale response. To that end, we will compare the probabilistic description of a desired QOI resulting from solving stochastic boundary value problems on a domain with two different resolutions of randomness. The coarse scale representation,

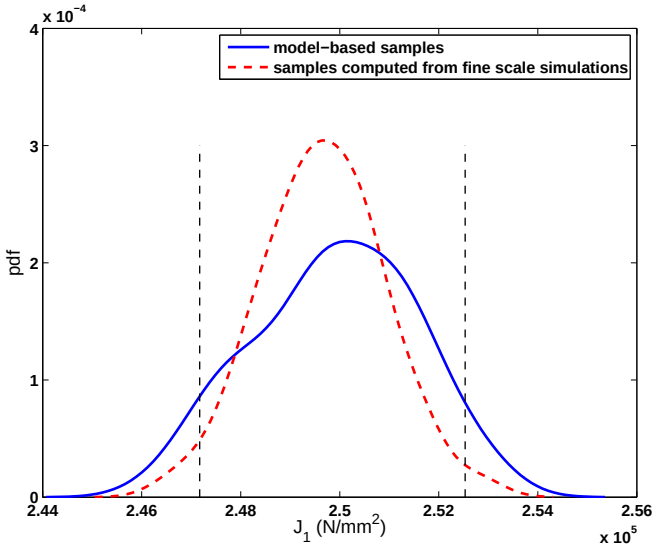

FIG. 8: Plot of the pdf's of $\mathbf{J}_1 = \mathrm{tr}([\mathbf{C}])$ estimated using the samples obtained from the probabilistic mesoscale model (solid blue line) and the observations computed from fine scale simulations (dashed red line). The results show that approximately 96% of the observations fall in the 95% confidence interval (black dashed line) of model predictions.

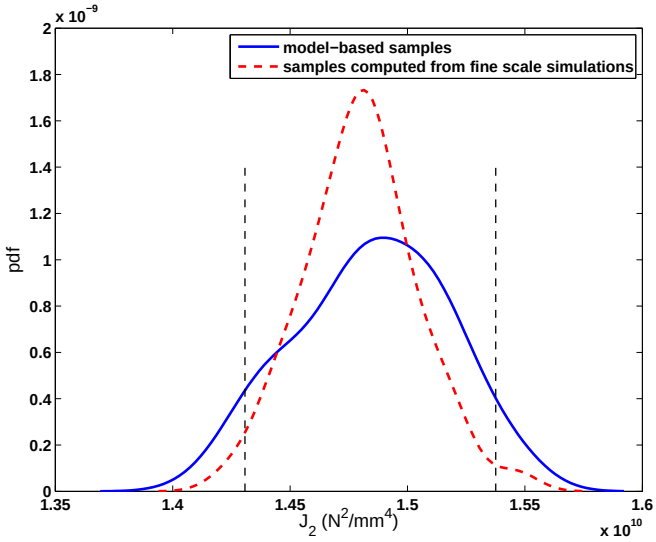

FIG. 9: Plot of the pdf's of $\mathbf{J}_2 = 1/2([\mathbf{C}]_{ii}[\mathbf{C}]_{jj} - [\mathbf{C}]_{ij}[\mathbf{C}]_{ji})$ estimated using the samples obtained from the probabilistic mesoscale model (solid blue line) and the observations computed from fine scale simulations (dashed red line). The results show that approximately 98% of the observations fall in the 95% confidence interval (black dashed line) of model predictions.

with mesoscale randomness, is constructed with reference to the probabilistic model of mesoscale elasticity tensor. The fine scale representation, with microscale randomness, is obtained making use of the statistical model of polycrystalline microstructure developed in Section 2. The fine scale responses are treated as observations with respect to which the model validation is exercised. The validation task will be investigated for the static as well as the dynamic case, i.e., the elastic wave response of the model to the ultrasonic excitation.

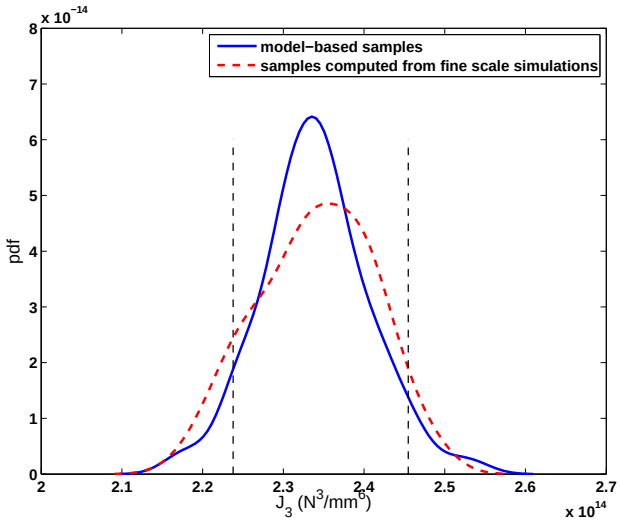

FIG. 10: Plot of the pdf's of $\mathbf{J}_3 = \det([\mathbf{C}])$ estimated using the samples obtained from the probabilistic mesoscale model (solid blue line) and the observations computed from fine scale simulations (dashed red line). The results show that approximately 96% of the observations fall in the 95% confidence interval (black dashed line) of model predictions.

TABLE 1: Second-order statistics, mean and coefficient of variation, of qualities of interest for both model-based samples and fine scale simulations

	$\mathbf{J}_1$		$\mathbf{J}_2$		$\mathbf{J}_3$	
	Mean	Cov	Mean	Cov	Mean	Cov
Model-based samples	2.497×10^5	0.0049	1.480×10^{10}	0.0161	2.341×10^{14}	0.0301
Fine scale simulations	2.499×10^5	0.0064	1.485×10^{10}	0.0214	2.339×10^{14}	0.0283

4.2 Validation Statement for Static Response

For the purpose of validation, we consider the open bounded domain $\mathcal{D} =]0,3[\times]0,3[$ (in mm) in $\mathbb{R}^2$. Null displacement Dirichlet boundary conditions are applied to the boundary $\partial\mathcal{D}^1$ defined as $\partial\mathcal{D}^1 = \{\mathbf{x} \in \mathcal{D} | x_2 = 0\}$, while a static load pressure $(0, 1000)$ (in megapascals) is applied at the free edge $\partial\mathcal{D}^2 = \{\mathbf{x} \in \mathcal{D} | x_2 = 3\}$. The fine scale resolutions of domain $\mathcal{D}$ is defined with reference to Voronoi-G polycrystal and constructed using the procedure discussed in Sections 2.2 and 2.3. Each realization of constructed polycrystals consists of approximately 180 grains. The domain is discretized using triangular isoparametric finite elements. The response of the fine scale representation is considered as model-based measurements for the purpose of validation. The coarse scale resolutions of domain $\mathcal{D}$ are the continuum mechanics model with mesoscopic randomness. The domain consists of $5 \times 5 = 25$ uniform regions such that the size of each region is consistent with the size of the SVE for which the probabilistic model of bounded elasticity tensor has been calibrated. Samples of apparent elasticity matrices are obtained by performing numerical Monte Carlo simulations of the random matrix $[\mathbf{C}]$ that are independently assigned to each region. The entire domain is then discretized into $45 \times 45 = 90$ quadratic finite elements as shown in Fig. 11. The response of the coarse scale representation forms the predictions of the candidate model. The validation task is then exercised by depicting and comparing the probabilistic description of the QOI, in form of pdf's, for both fine and coarse scale descriptions.

Let $\mathbf{x} \mapsto \boldsymbol{\sigma}(\mathbf{x})$ and $\mathbf{x} \mapsto \boldsymbol{\epsilon}(\mathbf{x})$ be the stress and strain random fields, respectively, resulting from solving the stochastic boundary value problem for both fine and coarse scale representations, with $N_{mc} = 500$ Monte Carlo simulations. As the quantity of interest, the volume averaged strain energy density $\varphi = (1/2)\langle\boldsymbol{\epsilon}(\mathbf{x})^T\boldsymbol{\sigma}(\mathbf{x})\rangle_V$ is

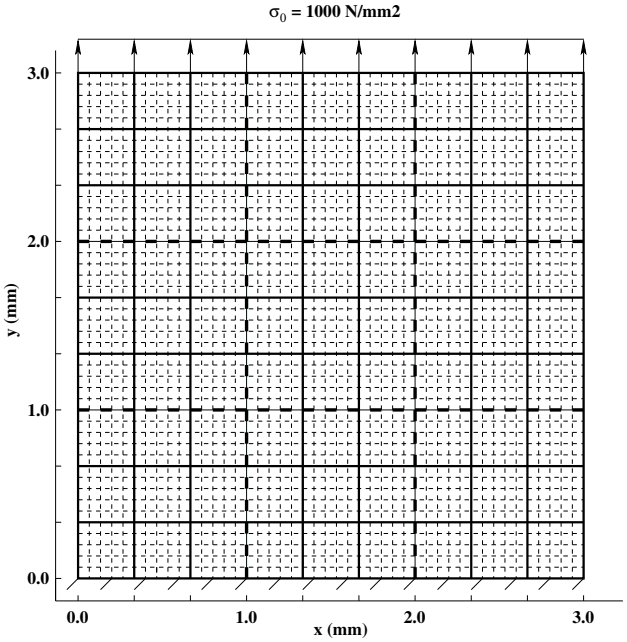

FIG. 11: Typical realization of the coarse scale representation of the domain $\mathcal{D}$ in the static case. The domain is discretized using 45×45 4-node quadratic elements; SVEs are shown with solid lines, and the thick dashed lines divide the domain into the subvolumes over which the local averaging is performed.

computed, where $V \subseteq \mathcal{D}$ is the domain over which the averaging is performed. Based on N_{mc} samples of fine and coarse scale models, estimates of pdf's of φ are obtained. The comparison of two pdf's is shown in Fig. 12, where the

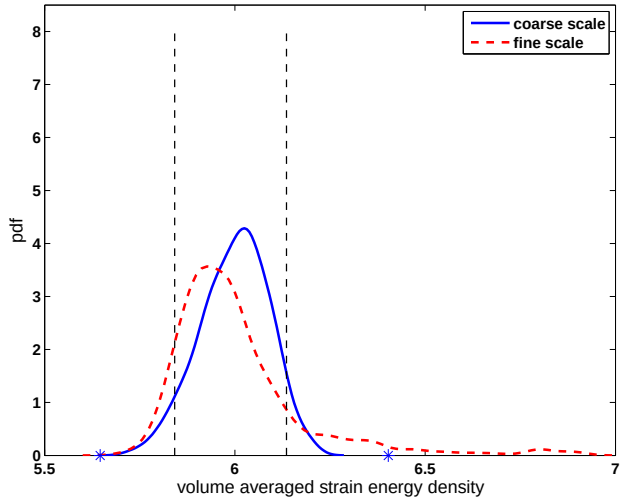

FIG. 12: Plot of the pdfs of volume averaged strain energy, $\varphi = (1/2)\langle \boldsymbol{\epsilon}(\mathbf{x})^T \boldsymbol{\sigma}(\mathbf{x}) \rangle_V$, over the entire domain; The dashed red line corresponds to the fine scale representation of domain $\mathcal{D}$ generated using the statistical model in Section 2. The solid blue line corresponds to the coarse scale representation of domain $\mathcal{D}$ using the probabilistic model for mesoscale elasticity tensor in Section 3. The 95% confidence intervals for the model predictions are shown as black dashed lines. The values of QOI obtained using the upper and lower bounds [Eqs. (56) and (57)] are marked with "$*$."

strain energy is averaged over the entire domain, i.e., $V = \mathcal{D}$. The result confirms that the predictions of the coarse scale model are in good agreement with the fine scale response. Approximately 80% of fine scale observables belong to the 95% confidence interval shown on the plot as black dashed lines. The mean and coefficient of variations of φ estimated from fine scale response are 6.006 and 0.030, respectively. These quantities are estimated to be 5.999 and 0.015 based on the coarse scale response. The values of QOI obtained from using the lower and upper bounds for mesoscale elasticity tensor [Eqs. (56) and (57)] are shown in the plot. These values are consistent with the estimated pdf of the coarse scale model.

In order to assess the credibility of the model in predicting the local response, the strain energy is also averaged over a set of subdomains $\{V_{ij}\}_{i,j=1}^{3}$ obtained from $3\times 3 = 9$ uniformly partitioning of $\mathcal{D}$ (thick dashed line in Fig. 11). The resulting pdf's are illustrated in Fig. 13. In most cases the fine scale observations validate the prediction of the coarse scale model, except when the averaging is performed over the region adjacent to the fixed boundary in which there is much more variation in the response of the microstructure. This could be due to the large variation in the stress and strain localization near the fixed boundary in the fine scale response. These local effects are the result of the fluctuations in the material properties at finer (microscopic) scales which are smoothed at the mesoscale during the calibration process. Consequently, these fluctuations cannot be propagated to the response of the coarse scale domain with mesoscopic randomness. In this case the model predictions are mostly concentrated around the mean response of the fine scale representation.

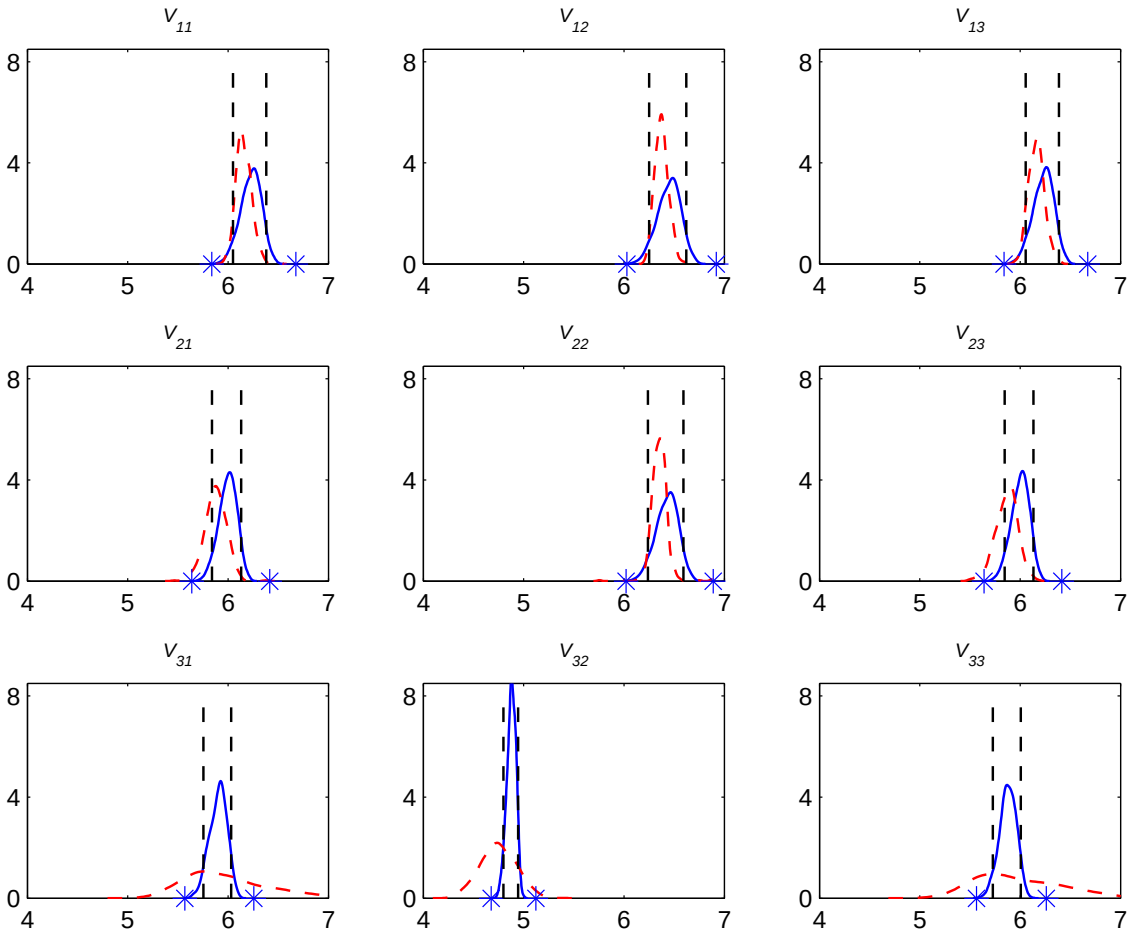

FIG. 13: Plot of the pdf's of volume averaged strain energy corresponding to the subvolumes $\{V_{ij}\}_{i,j=1}^{3}$ separated by thick dashed line in Fig. 11 (see the caption to Fig. 12 for the references to color in this figure legend).

4.3 Validation Statement for Ultrasonic Wave Response

In this section we exercise the validation of the identified probabilistic model in Section 3, when it is used to predict the desired response in elastodynamic regime. At this stage, we point out that the construction of the random matrix model for bounded elasticity tensor relies on assumptions that are valid within the range of linear elastostatic regime. In particular, the proof of the boundedness constraints, obtained using Huet's partitioning technique, relies on the energy theorems in elastostatics. As such, using the energy-based bounds is not well justified beyond the static regime from a theoretical point of view. Also, from the perspective of homogenization theory, overall dynamic moduli are generally different from overall static moduli. Nevertheless, we would like to examine the validity of the model, beyond its range of theoretical assumptions, when it is used as a predictive tool for ultrasonic wave response.

Nondestructive evaluation (NDE) using ultrasonic waves is extensively used in solid media to assess the quality of the structural and mechanical components during their manufacturing and lifetime. The applications in the metallic structure include characterization of material properties, detection of flaws, and evaluation of degradation during service life, to name a few. When an elastic wave propagates through a heterogeneous material, the ultrasonic energy is dispersed and scattered in many directions due to the interaction with heterogeneities. The scattering is often characterized by attenuation, which reflects the rate of dissipation in the intensity or the amplitude of the incident wave. Thus, as the QOI, we look at the attenuation coefficient which quantifies the dissipation of wave energy as it interacts with the heterogeneity.

Let the domain $\mathcal{D} \subset \mathbb{R}^2$ be the open bounded region of $]0,6[\times]0,6[$ (in millimeters) with displacement-free boundary conditions over the entire boundary $\partial\mathcal{D}$. A point source excitation is applied at the point of coordinates $(3,3)$ (in millimeters) in the $\mathbf{e}_2$-direction in the form of a Ricker pulse in the time domain to model the incident wave. Similar to Section 4.2, finite element models of both fine and coarse scale resolutions of domain $\mathcal{D}$ are constructed. The fine scale representation in this case consists of approximately 800 grains and is discretized using approximately 140,000 triangular elements. The coarse scale representation consists of 20×20 SVEs and is discretized into $200 \times 200 = 400$ quadratic finite elements. For both fine and coarse scale representations, the stochastic waveforms corresponding to the displacement in $\mathbf{e}_2$-direction are computed in an array of nine equally spaced receivers by solving the stochastic boundary value problem in the time domain with $N_{mc} = 100$ Monte Carlo simulations. The location of the source and the receivers on a typical realization of the coarse scale domain is illustrated in Fig. 14. For the dynamic analysis, the constant value of 2700 (in kg/m^3) is assumed for the density of aluminum polycrystal throughout the domain.

Let $(\mathbf{x},t) \mapsto \mathbf{v}(\mathbf{x},t) = [v_1(\mathbf{x},t), v_2(\mathbf{x},t)]$ denote the resulting $\mathbb{R}^2$-valued displacement random field. The amount of energy in the waveforms can be characterized by the intensity $\mathbf{x} \mapsto \mathbf{I}(\mathbf{x}) = [I_1(\mathbf{x}), I_2(\mathbf{x})]$ defined by

$$\mathbf{I}(\mathbf{x}) = \int_\tau \mathbf{v}^2(\mathbf{x},t)dt, \tag{65}$$

where τ is the time period of duration of the wave. Let $\{v_2(\mathbf{x}^i,t)\}_{i=1}^9$, where $\mathbf{x}^i$ is the location of receiver i, be the set of stochastic processes of resulting waveforms in the $\mathbf{e}_2$-direction at nine receivers. The corresponding set of wave intensities is denoted as $\{I_2(\mathbf{x}^i)\}_{i=1}^9$. For each realization of a set of waveforms, the corresponding estimate of attenuation coefficient α is obtained by fitting these values to the best exponential decay function of the form $I_2^o e^{-2\alpha\|\mathbf{x}^i - \mathbf{x}^o\|}$, where $\mathbf{x}^o$ and I_2^o are the location and the intensity of the source wave, respectively. A typical plot of fitting the exponential decay function to the computed values of intensity is illustrated in Fig. 15. The estimates of pdf's of QOI, the attenuation coefficient, are obtained from N_{mc} realizations of α for both fine and coarse scale domains. These pdf's are compared in Fig. 16 for three different central frequencies of the source excitation, $f_c = 2, 5, 10$ (in megahertz). It is seen that in this case the predictions of the model always belong to a subset of the observations. There is much smaller variation in the model predictions relative to the fine scale response. This is expected since the wave scattering regime is very sensitive to the length scale of the heterogeneity in the medium. For the lower frequency regime, $f_c = 2$ (in megahertz), where the wave propagates over a larger length scale as compared to the length scale of heterogeneity, we have a quasistatic regime. Hence, the bounds on apparent elasticity matrix may be still valid and the predictions of the coarse scale model in this case are more consistent as they fall around the mean response. Obviously as we

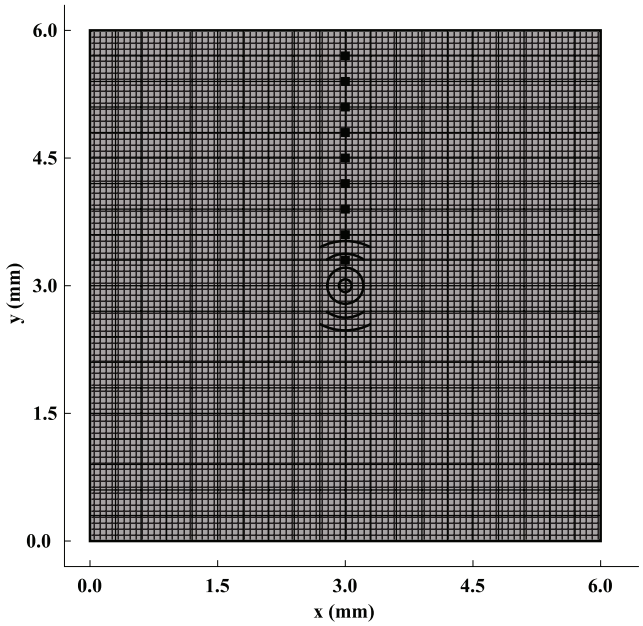

FIG. 14: Typical realization of coarse scale domain for dynamic case consisting of 20×20 SVEs (separated by thin solid lines). The entire domain is discretized into $200 \times 200 = 400$ quadratic finite elements. A point source is generated at the center of the domain and the resulting waveforms in an array of nine receivers (black squares) are used to compute the attenuation coefficient.

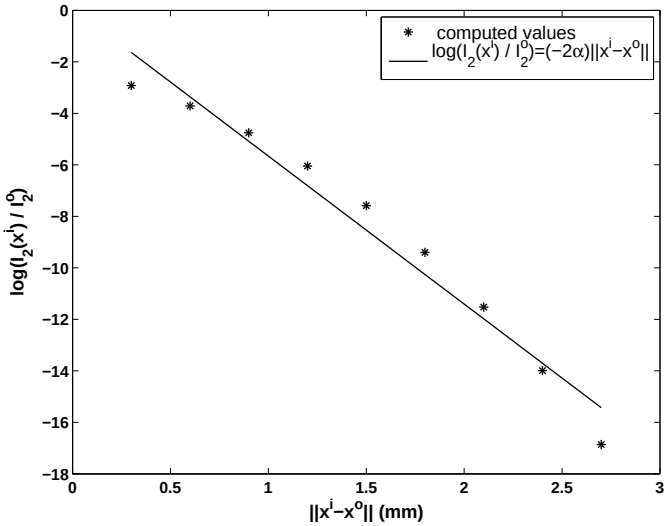

FIG. 15: Typical plot illustrating the estimation of the attenuation coefficient α; the exponential decay function of the form $I_2^o e^{-2\alpha\|\mathbf{x}^i-\mathbf{x}^o\|}$ (solid line) is fitted to the computed values of intensity ($*$) in an array of nine receivers.

increase the frequency of excitation, not only the attenuation is more sensitive to subscale heterogeneity which cannot be captured by the mesoscale model, but also the bounds becomes more inconsistent with the physics. This can explain more significant modeling biases observed in the results corresponding to the central frequencies of $f_c = 5$ and 10 (in megahertz).

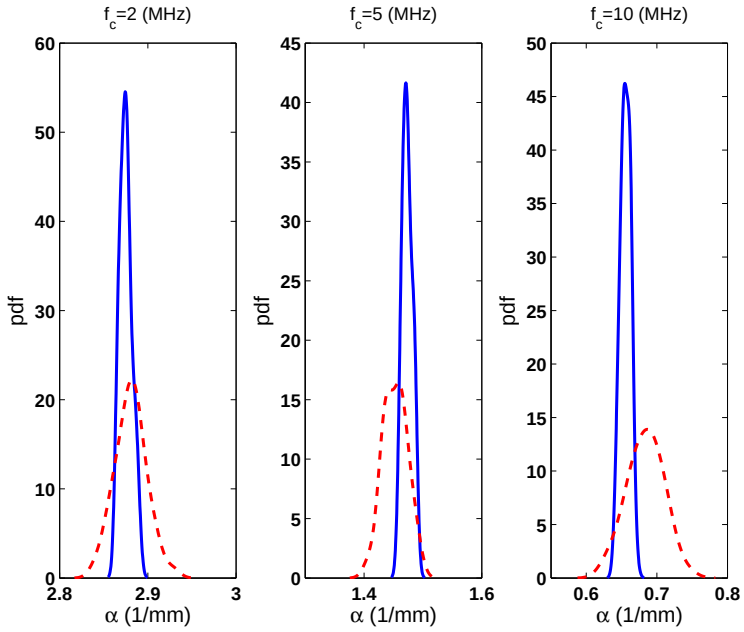

FIG. 16: Estimates of pdf's of attenuation coefficient α for three different central frequency of excitations, $f_c = 2, 5, 10$ mHz; the coarse scale (solid line) and the fine scale (dashed line).

5. CONCLUDING REMARKS

In this paper, we have addressed the validation of a predictive model for the mesoscale elastic behavior of materials with microstructures. We first presented a procedure for summarizing experimental data from microstructural measurements in order to develop a statistical model for characterization and realizations of polycrystalline microstructures. The model provides an efficient tool to digitally generate realizations of microstructures in accordance with the available data and is utilized to ensure a reasonable level of convergence in the process of identification of the probabilistic model of the coarse scale material description. It is also employed in the validation stage for the purpose of generating model-based observations. We then recalled the construction of the candidate probability model for the mesoscopic description of mechanical system. The linear elastic constitutive matrix of this model is described mathematically as a bounded matrix-valued random variable. The bounds reflect theoretical bounds consistent with the theory of elasticity.

We first verify the calibration process by validating the model in the regime of behavior where the calibration was conducted. The results confirm a high level of confidence in the performance of the model when it is used to take into account physical phenomena occurring at the calibration scale. The model validation was then studied from the perspective of intended uses of the model. For this purpose, we solved stochastic boundary value problems using Monte Carlo simulations for a domain with two different resolutions of randomness. The fine scale representation, with microscale randomness, is obtained using the statistical model for simulation of microstructures developed in the first part of the paper. This representation is used to generate the model-based measurements. The coarse scale representation, with mesoscale randomness, is defined with reference to the identified probabilistic model of mesoscale elasticity tensor. We investigated the predictive accuracy of the model predictions by comparing the probability density functions of a desired response quantity of interest estimated from both coarse and fine scale representations. Based on the results, the stochastic model of the mesoscale elasticity tensor is found to be adequate to predict the response quantity of interest in the static regime. Approximately 80% of simulated data, obtained using subscale simulations, are found to belong to the 95% confidence interval of model predictions. The variation in the model predictions is adequately consistent with the fine scale response. The validation task was also examined for the case of ultrasonic

wave response. It is found that in this case the model predictions belong only to a subset of possible behaviors. This could be because the boundedness constraints in the construction of the model are defined with respect to the elastostatic behavior. Also the model predictions are not able to adequately account for the fine scale randomness since the scattering behavior is very sensitive to fine scale fluctuations, which are smoothed at the mesoscale during the calibration procedure. The predictions of the model are more consistent with the mean response for the lower frequency where we have a quasistatic regime, and hence the bounds on the apparent elasticity matrix may be still valid. More research is required to define appropriate physics-based bounds on apparent elasticity tensor that are consistent with the dynamic regime in higher frequencies.

The quantification of damage requires sensor information being interpreted in terms of hierarchy of damage accumulation models, which effectively represent the material and structural changes that occur during the lifetime of the system. The proposed probabilistic model combined with the finite element analysis can be used as a predictive tool in the system level in the context of structural health monitoring and damage prognosis. The sensitivity of the model to the subscale heterogeneity is the key to its applicability in predicting phenomena occurring at the damage initiation scale.

ACKNOWLEDGMENTS

This work was supported by an MURI administered by AFOSR on Health Monitoring and Materials Damage Prognosis for Metallic Aerospace Propulsion and Structural Systems, under grant no FA95550-06-1-0309, David Stargel, program manager. The work of the third author was funded by the French Research Agency (Agence Nationale de la Recherche) under TYCHE contract no ANR-2010-BLAN-0904.

REFERENCES

1. Hill, R., The elastic behaviour of a crystalline aggregate, *Proc. Phys. Soc.*, London, Sect. A., 65:349, 1952.
2. Hill, R., Elastic properties of reinforced solids: Some theoretical principles, *J. Mech. Phys. Sol.*, 11(5):357–372, 1963.
3. Hashin, Z. and Shtrikman, S., A variational approach to the theory of the elastic behaviour of multiphase materials, *J. Mech. Phys. Sol.*, 11(2):127–140, 1963.
4. Kroner, E., *Statistical continuum mechanics*, Springer, Berlin, 1972.
5. Kroner, E., Bounds for effective elastic-moduli of disordered materials, *J. Mech. Phys. Sol.*, 25(2):137–155, 1977.
6. Willis, R., Variational and related methods for the overall properties of composites, *Adv. Appl. Mech.*, 21:1–78, 1981.
7. Nemat-Naser, S. and Hori, M., *Statistical Continuum Mechanics*, North-Holland, Amsterdam, 1993.
8. Huet, C., Application of variational concepts to size effects in elastic heterogeneous bodies, *J. Mech. Phys. Sol.*, 38(6):813–841, 1990.
9. Soize, C., A nonparametric model of random uncertainties on reduced matrix model in structural dynamics, *Probab. Eng. Mech.*, 15(3):277–294, 2000.
10. Soize, C., Maximum entropy approach for modeling random uncertainties in transient elastodynamic, *J. Acous. Soc. Am.*, 109(5):1979–1996, 2001.
11. Guilleminot, J., Noshadravan, A., Soize, C., and Ghanem, R., A probabilistic model for bounded elasticity tensor random fields with application to polycrystalline microstructures, *Comput. Methods Appl. Mech. Eng.*, 200:1637–1648, 2011.
12. Adams, B. L., Orientation imaging microscopy: Application to the measurement of grain boundary structure, *Mater. Sci. Eng.: A*, 166:59–66, 1993.
13. Schwartz, A. J., Kumar, M., Field, D. P., and Adams, B. L., *Electron Backscatter Diffraction in Materials Science*, Kluwer Academic, Dordrecht, 2000.
14. Garcia, M. P., Luo, C., Noshadravan, A., Keck, A., Teale, R., Chattopadhyay, A., and Peralta, P., Microstructure representation and material characterization for multiscale finite element simulations of local mechanical behavior in damaged metallic structures, *Proc. SPIE*, 6926, 69260K, 2008.
15. Bunge, H. J., *Texture Analysis in Materials Science: Mathematical Methods*, Butterworth-Heinemann, London, 1982.

16. Okabe, A., *Spatial Tessellations: Concepts and Applications of Voronoi Diagram*, Wiley Series in Probability and Statistics, Wiley, Chichester, UK, 2000.
17. Stoyan, D., Kendall, W., and Mecke, J., *Stochastic Geometry and Its Applications*, Wiley Series in Probability and Mathematical Statisitics, Applied probability and statistics, Wiley, Chichester, UK, 1987.
18. Starzewski, M. O., *Microstructural Randomness and Scaling in Mechanics of Materials*, CRC Series–Modern Mechanics and Mathematics, Chapman and Hall/CRC, London, 2008.
19. Arwade, S. and Grigoriu, M., Probabilistic model for polycrystalline microstructures with application to intergranular fracture, *J. Eng. Mech.*, 130(9):997–1005, 2004.
20. Scheike, T., Anisotropic growth of voronoi cells, *Ad. Appl. Probab.*, 26:43–53, 1994.
21. Green, P. and Sibson, R., Computing Dirichlet tessellations in the plane, *Comput. J.*, 21(2):168–173, 1978.
22. Kullback, S., *Information Theory and Statistics*, Dover Publications, New York, 1968.
23. Csiszár, I., Information-type measures of difference of probability distributions and indirect observation, *Stud. Sci. Math. Hung.*, 2:299–318, 1967.
24. Yamazaki, F. and Shinozuka, M., Digital generation of non-Gaussian stochastic fields, *J. Eng. Mech.*, 114:1183–1197, 1988.
25. Grigoriu, M., Simulation of stationary non-Gaussian translation process, *J. Eng. Mech.*, 124:121–126, 1998.
26. Popescu, R., Deodatis, G., and Prevost, J. H., Simulation of homogeneous non-Gaussian stochastic vector fields, *Probab. Eng. Mech.*, 13:1–13, 1998.
27. Phoon, K. K., Huang, S. P., and Quek, S. T., Simualtion of second-order processes using Karhunen-Loeve expansion, *Compuat. Struct.*, 80:1049–1060, 2002.
28. Sakamoto, S. and Ghanem, R., Polynomial chaos decomposition for the simulation of non-Gaussian nonstationary stochastic processes, *J. Eng. Mech.*, 128:190–201, 2002.
29. Grigoriu, M., Crossings of non-Gaussian translation processes, *J. Eng. Mech.*, 110:610–620, 1984.
30. Grigoriu, M., *Applied non-Gaussian Processes: Examples, Theory, Simulation, Linear Random Vibration, and MATLAB Solutions*, Prentice-Hall, Englewood Cliffs, NJ, 1995.
31. Li, L. B., Phoon, K. K., and Quek, S. T., Comparison between Karhunen-Loeve expansion and translation-based simulation of non-Gaussian processes, *Compuat. Struct.*, 85:264–276, 2007.
32. Fackler, P. L. and King, R. P., Generation of dependent random variates with given marginal distributions and fractile correlation structure. Selected paper presented at the AAEA meetings, Knoxville, TN, July 31-Aug 3, 1988. Abstract published in *Am. J. Agr. Econ.*, 70, 1988.
33. Hotelling, H. and Pabst, M. R., Rank correlation and tests of significance involving no assumption of normality, *Ann. Math. Stat.*, 7:29–43, 1936.
34. Loeve, M., *Probability Theory*, Springer-Verlag, New York, 4th edition, 1977.
35. Ghanem, R. and Spanos, P., *Stochastic Finite Elements: A Spectral Approach*, Springer, New York, 1991.
36. Soize, C., Random matrix theory for modeling uncertainties in computational mechanics, *Comput. Methods Appl. Mech. Eng.*, 194:1333–1366, 2005.
37. Soize, C., Non-Gaussian positive-definite matrix-valued random fields for elliptic stochastic partial differential operators, *Comput. Methods Appl. Mech. Eng.*, 195:26–64, 2006.
38. Soize, C., Tensor-valued random fields for meso-scale stochastic model of anisotropic elastic microstructure and probabilistic analysis of representative volume element size, *Probab. Eng. Mech.*, 23:307–323, 2006.
39. Das, S. and Ghanem, R., A bounded random matrix approach for stochastic upscaling, *SIAM Multiscale Model. Simul.*, 8(1):296–325, 2009.
40. Hazanov, S. and Huet, C., Order relationships for boundary conditions effect in heterogeneous bodies smaller than representative volume, *J. Mech. Phys. Solids*, 42(12):1995–2011, 1994.
41. Shannon, C. E., A mathematical theory of communication, *Bell Syst. Tech. J.*, 27:379–423 and 623–656, 1948.
42. Jaynes, E. T., Information theory and statistical mechanics, *Phys. Rev.*, 106(4):620–630, 1957.
43. Jaynes, E. T., Information theory and statistical mechanics, *Phys. Rev.*, 108(2):171–190, 1957.
44. Nagar, D. K. and Gupta, A., Matrix-variate Kummer-Beta distribution, *J. Austral. Math. Soc.*, 73:11–25, 2002.

45. Guilleminot, J. and Soize, C., Probabilistic modeling of apparent tensors in elastostatics: A maxent approach under material symmetry and stochastic boundedness constraints, *Probab. Eng. Mech.*, 28:118–124, 2012.
46. Mahadevan, S. and Rebba, R., Validation of reliability computational models using Bayes networks, *Reliab. Eng. Syst. Saf.*, 87(2):223–232, 2005.
47. Rebba, R., Huang, S., Liu, Y., and Mahadevan, S., Statistical validation of simulation models, *Int. J. Mater. Product Technol.*, 25:164–181, 2006.
48. Ghanem, R., Doostan, A., and Horse, J. R., A probabilistic construction of model validation, *Comput. Methods Appl. Mech. Eng.*, 197:2585–2595, 2008.